

(4)



AD-A133402

STANFORD/NASA AMES JOINT INSTITUTE FOR SURFACE AND MICROSTRUCTURE RESEARCH
DEPARTMENT OF MATERIALS SCIENCE AND ENGINEERING
STANFORD UNIVERSITY
STANFORD, CA 94305

FABRICATION AND PROPERTIES OF MULTILAYER STRUCTURES

prepared by

W. A. Tiller

September 1983

SU-DMS-83-R-5

DTIC FILE COPY

Final Technical Report for Period 1 September 1981 - 30 September 1982
(Contract #MDA903-81-C-0578)

prepared for

ADVANCED RESEARCH PROJECTS AGENCY
1400 Wilson Boulevard
Arlington, VA 22209

DTIC
SELECTED
S OCT 07 1983 D
E

Department of MATERIALS SCIENCE AND ENGINEERING
STANFORD UNIVERSITY

This document has been approved
for public release and sale; its
distribution is unlimited.

83 09 26 044

FINAL TECHNICAL REPORT
ON
FABRICATION AND PROPERTIES OF
MULTILAYER STRUCTURES

1 September 1981 - 30 September 1982

This research was sponsored by the
Defense Advanced Research Projects
Agency under ARPA Order No. 3706
Contract No. MDA903-81-C-0578
Monitor: ONR Resident Representative

Contractor: Stanford University

Effective Date of Contract: September 1, 1981

Contract Expiration Date: September 30, 1982

Principal Investigator: William A. Tiller

Phone: (415) 497-3901

Stanford/NASA Ames Joint Institute for Surface and Microstructure Research
Department of Materials Science and Engineering
Stanford University, Stanford, CA 94305

REPORT DOCUMENTATION PAGE		READ INSTRUCTIONS BEFORE COMPLETING FORM	
REF ID: NUMBER SU-DMS-83-R-5	12. GOVT ACCESSION NO. AD-A133402	13. RECIPIENT'S CATALOG NUMBER	
4. TITLE (and Subtitle) FABRICATION AND PROPERTIES OF MULTILAYER STRUCTURES		5. TYPE OF REPORT & PERIOD COVERED Final Report (9/1/81 - 9/30/82)	
7. AUTHOR(s) W. A. Tiller		6. PERFORMING ORG. REPORT NUMBER MDA903-81-C-0578,	
9. PERFORMING ORGANIZATION NAME AND ADDRESS Ames Joint Institute for Surface and Microstructure Research, Department of Materials Science & Engrg., Stanford University, Stanford, CA 94305		10. PROGRAM ELEMENT, PROJECT, TASK AREA & WORK UNIT NUMBERS	
11. CONTROLLING OFFICE NAME AND ADDRESS Advanced Research Projects Agency (ARPA) 1400 Wilson Boulevard Arlington, VA 22209		12. REPORT DATE September 1983	
		13. NUMBER OF PAGES 46	
14. MONITORING AGENCY NAME & ADDRESS (if different from Controlling Office)		15. SECURITY CLASS. (of this report) UNCLASSIFIED	
		15a. DECLASSIFICATION/DOWNGRADING SCHEDULE	
16. DISTRIBUTION STATEMENT (of this Report) Unlimited Distribution			
17. DISTRIBUTION STATEMENT (of the abstract entered in Block 20, if different from Report)			
18. SUPPLEMENTARY NOTES This contract is awarded under Basic Agreement No. 12740-01-00 dated 81-09-01, amended by modifications P00001 and P00002, issued by the Office of Naval Research. This research is sponsored by the Defense Advanced Research Projects Agency (DARPA).			
19. KEY WORDS (Continue on reverse side if necessary and identify by block number) REACTIVE SPUTTERING, FILM FORMATION, SILICON DIOXIDE, SILICON CARBIDE, SEMI-CONDUCTOR PROCESSING, THERMAL OXIDATION, INTERSTITIAL SPECIES, CRYSTALLOGRAPHY, MOLECULAR ORBITALS, AMORPHOUS FILMS, INTEGRATED CIRCUITS, COMPUTER SIMULATION <i>15a. X</i>			
20. ABSTRACT (Continue on reverse side if necessary and identify by block number) The synthesis of SiC films and Pd_2Si films via single source and dual source sputtering, respectively, has been experimentally investigated while the reactive sputter deposition of SiO_x films has been theoretically analyzed. The SiO_x film data requires a mobile precursor adsorption process to be operative for the oxygen and an oxygen sticking coefficient of between 1.56×10^{-3} and 4.17×10^{-3} . An			

analysis of in-situ electrical diagnostics of the films via a non-contact technique shows the method to be of marginal accuracy for the example selected.

An important new formulation of the stress and elastic constant tensors in the vicinity of interfaces has been developed and applied to the simple example of adsorbed layer/substrate interactions via a parametric analysis. Atomic modeling of the SiO system yields peroxide bond formation for oxygen-rich (100) α -cristobalite surfaces. Radial distribution function and angular distribution function data have been calculated for bulk α -quartz and bulk α -cristobalite in good agreement with experiment. ↵

Accession For	
NTIS GRA&I	<input checked="" type="checkbox"/>
DTIC TAB	<input type="checkbox"/>
Unannounced	<input type="checkbox"/>
Justification	
By	
Distribution/	
Availability Codes	
Dist	Avail. Indiv. or Special
A	



UNCLASSIFIED

INTRODUCTION

This report focuses on five individual work areas: (i) synthesis of SiO_x , (ii) synthesis of SiC, (iii) synthesis of Pd_2Si , (iv) electrical diagnostics of films and (v) computer modeling of film synthesis.

Reactive sputter deposition of refractory oxides, under conditions in which the reaction between the sputtered species and the oxygen is isolated to the deposition surface, has been experimentally investigated. Results for the formation of $\text{SiO}_x(0 \leq x \leq 2)$ under such experimental conditions are discussed below. It is shown that the dependence of the deposited film stoichiometry on oxygen pressure and the incidence rate of silicon can be correlated with reported results of oxygen adsorption onto single crystal silicon surfaces and amorphous silicon surfaces. This correlation is made in terms of oxygen exposure, $L(\text{Torr-sec})$. For our work, a dynamic exposure, L_D , is defined for steady state synthesis conditions by placing the origin of a moving reference frame at the deposition surface. By means of this correlation, it is found that the sticking coefficient of oxygen onto room temperature substrates is dependent of oxygen coverage (i.e., surface stoichiometry) for coverages less than 0.8. This requires that a mobile precursor adsorption process be operative for oxygen in our experiments.

The reactive sputtering study was briefly extended to an N_2 environment and conditions for the formation of Si_3N_4 determined. In the SiC work, the emphasis was on high substrate temperature depositions where surface contamination and surface conversion of Si to SiC was observed.

Much effort was spent on high temperature development and on maintenance of a clean environment in this high temperature domain. Steady, rather than dramatic, progress is being made.

Using the phase spread technique and a room temperature substrate, the structural character of the films as a function of composition in the Pd-Si system have been determined. In the electrical diagnostics of films area, an analysis has been made of the proposed measurement technique for the specific case of in-situ film monitoring during oxidation. The results indicate that the technique is only marginal with respect to sensitivity revealing interface capacitance and interface resistance effects.

In the theoretical section, an important new formulation of the stress and elastic constant tensors in the vicinity of interface is given. This is applied to the simple example of an absorbed layer/substrate interaction system. For the Si-O system, radial distribution function and angular distribution data have been generated for bulk α -quartz and α -cristobalite while surface reconstruction producing peroxide bond formation has been found for the (100) α -cristobalite surface.

A. Experimental Results

1. Reactive Sputter Deposition of Oxide and Nitride Films

SiO_x - The Silicon-Oxygen System Analysis

Reactive sputter deposition of refractory oxides, under conditions in which the reaction between the sputtered species and the oxygen is isolated to the deposition surface, has been experimentally demonstrated and reported on in many previous reports⁽¹⁾. The experimental results presented demonstrate that the synthesis of silicon-oxygen films under controlled conditions, designed so that reaction between silicon and oxygen

occurs at the deposition surface, allows formation of films of reproducible stoichiometry and high uniformity onto room temperature substrates. To date, we have discussed these results in terms of the relative rates of incidence of the two reacting species onto the deposition surface. It is important at this point to consider experimental results reported by other investigators concerning the adsorption of oxygen onto surfaces of bulk single crystals and of amorphous silicon. Such surfaces are static in that the number of Si atoms is fixed by the character of the initial surface. In our experiments, a dynamic moving surface is studied in which both silicon and oxygen are supplied to a moving surface, i.e., a film is being grown.

More sophisticated experiments in which ultra high vacuum studies of oxygen absorption on high index silicon planes (2,3,4) and amorphous silicon⁽⁵⁾ have been reported. In these studies the oxygen is observed to be absorbed with the coverage being a linear function of oxygen exposure in Langmuirs (torr-sec). Sticking probabilities are small (2×10^{-4} to 3×10^{-3}) and are strongly affected by the presence of excited oxygen. Additionally, the oxygen is absorbed in an unreacted state. This reaction ($Si + O_2 \rightarrow SiO_2$) is apparently strongly catalyzed⁽⁴⁾ by the presence of small amounts of carbon. Adsorption on amorphous silicon does not appear to be substantially different from absorption on (111) or (110) silicon surfaces. The sticking coefficient of oxygen on silicon (111) and (110) surfaces were reported to be 2×10^{-4} and 6×10^{-3} respectively. The higher value on (110) surface can be explained by its higher index and the possibility of surface step effects.

In this work⁽¹²⁾ the sticking coefficient, S , was determined by analysis of experimental data obtained using Auger Electron Spectroscopy⁽²⁾

4) (AES), High Resolution Electron^(2,3) Spectroscopy (HRES), and Ellipsometry^(2,3) (E). It was assumed in all these experiments that the coverage, θ , was directly proportional to the intensity of the signal monitored which was determined as a function of oxygen exposure, L , and that unit coverage was produced when the experimental signal saturated. Under these assumptions the coverage dependence of the sticking coefficient $S(\theta)$ could be derived as

$$\frac{d}{dt}(\theta) = S(\theta) \frac{vP}{N_0} \quad (1)$$

where θ is the fractional coverage, P the pressure, $v = 3.48 \times 10^{20}$ molecule/cm² - sec Torr and N_0 the number of surface sites available for absorption.

The relationship between coverage, θ , and exposure is similar to the relationship between composition and relative rates of incidence shown in Fig. 1. A more direct comparison can be made if our data is displayed in terms of the oxygen concentration given as X in SiO_x with $0 < X < 2$ and a dynamic exposure L_D . The correspondence between coverage, θ , and X in SiO_x is straight-forward if we assume that the absorbed species is O_2 and that unit coverage is attained when there is one oxygen molecule absorbed for each silicon surface atom.

Dynamic exposure, L_D , is defined by the time necessary to deposit a monolayer of silicon atoms which is used in the calculation of oxygen exposure at pressure P . The number of atoms on an exposed (111) silicon surface is calculated to be $\sim 3.96 \times 10^{14}/\text{cm}^2$. The rate of incidence of silicon atoms, v_{Si} , has been already given as $v_{\text{Si}} = R_{\text{Si}}/V_{\text{Si}}$ where R_{Si} is the deposition rate in A^3/sec and V_{Si} and V_{Si} is atomic volume of

silicon. The time τ , to deposit one monolayer, i.e. 3.96×10^{14} atoms/cm² is then

$$\tau = \frac{3.96 \times 10^{14}}{v_{Si}} = \frac{3.96 \times 10^{14} v_{Si}}{R_{Si}} \quad (2)$$

Thus, a dynamic exposure L_D for oxygen can be defined as

$$L_D = P_{O_2} \tau \quad (3)$$

where P_{O_2} is given in torr and τ in seconds. During a steady state synthesis experiment static exposure and dynamic exposure are analytically equivalent at small time steps.

our experimental results are plotted as X in SiO_x versus dynamic exposure L_D in Fig. 2. The results of Ritter⁽⁸⁾ are also plotted for comparison. The differences are striking. First, the dynamic exposure range, in Langmuirs, over which our data extends is approximately 10^{-4} to 10^{-3} L. In order to gain the same results, Ritter's range was approximately $10^{-8}L$ to $10^{-2}L$. No clear explanation for this appears in the data of either investigation. It is likely, though, that Ritter's⁽⁶⁾ work had substantial amounts of excited oxygen present. The absorption and reaction probability of excited O_2 is orders of magnitude higher than unexcited O_2 . Therefore, the reactivity of the oxygen in the evaporation experiment was undoubtedly strongly increased by the experimental arrangement used. In our work, the oxygen was introduced at the substrate in an unexcited state. The substrate to sputter source spacing was large enough that the coupling between the plasma and the deposition surface was minimal (a characteristic of planar magnetron systems). Additionally,

substrate heating, consistent with the deposition parameters ($T_s < 65^{\circ}\text{C}$) was observed for extended synthesis experiments (< 2 hrs) substantiating that the source-substrate coupling was minimal.

It is informative to compare coverage^(2,3) as determined by E, HRES and AES with our data for X in SiO_x versus exposure, L_D , as shown in Fig. 3. The qualitative behaviors are very similar and quantitative agreement occurs with respect to the exposure range involved (i.e., 10^{-4} to 10^{-3} torr-sec). This implies that the rate controlling step in the synthesis process is identical to that in the absorption process of O_2 in silicon. Hence, our rate controlling step is the absorption of O_2 with reaction to form SiO_x occurring once the absorption step has taken place.

The slopes of the film stoichiometry curves (X in SiO_x) are steeper than the absorption curves implying a somewhat larger sticking coefficient. When plotted in a linear manner, Fig. 4, the relationship between X in SiO_x is observed to be a linear function of exposure without experimental scatter. This states that the sticking coefficient of oxygen is independent of coverage, a condition which occurs when there is a mobile precursor to the chemisorption event. Therefore, it is quite likely that, in our work, a mobile precursor of O_2 adsorbed onto the surface exists and facilitates the chemisorption process.

A sticking coefficient, S , for O_2 onto our moving deposition surface can also be estimated for these data. If we assume unit coverage, when $X = 2$ for X in SiO_x , the coverage can be linearly related to X by $\theta = X/2$. At constant pressure, P , the time rate of change of the coverage, $\dot{\theta}$, can be related (Eq. (1)) to the sticking coefficient, $S(\theta)$. The sticking coefficient derived on this basis is in the range 1.56×10^{-3} to 4.17×10^{-3} . These numbers are a factor of 5 to 20 larger than the value reported by

Ibach ($S = 2.2 \times 10^{-4}$) for an atomically flat (111) surface. This increase in S may be due either to the presence in our work of activated oxygen or to an enhanced reactivity of our amorphous SiO_x surface relative to ideal crystalline surfaces. The latter of these explanations is consistent with the effects of surface steps on the sticking probability. It would require 6-8% of the surface atoms to be associated with surface steps to achieve sticking probabilities as we have inferred. Computer simulation studies of amorphous surfaces by Garofolini et al⁽⁷⁾ tend to support this interpretation.

The observed independence of the sticking coefficient on θ , for O_2 on the silicon surface can be explained by a mechanism in which a physisorbed mobile precursor state for oxygen exists on the sample surface prior to the chemisorption. This allows O_2 molecules to move on the surface so that, at substantial coverages ($\theta = 0.5$), the remaining unoccupied chemisorption sites are accessible. A simple model⁽⁸⁾ of the combined physisorption-chemisorption process shows the sticking coefficient $S(\theta)$ for the chemisorbed stated to be given by

$$S(\theta) = \frac{\alpha(1 - \theta)}{(1 + r_d/r_c) - \theta(1 + r_d/r_m)^{-1}} \quad (4)$$

where θ is the coverage, α the fraction of incident gas molecules entering the precursor state, r_d the rate of desorption, r_m the rate of migration, and r_c the rate of transition from the precursor to the chemisorbed state. In the limit of $\theta \rightarrow 0$, the sticking coefficient S_0 is given by

$$S_0 = \frac{\alpha}{(1 + 4r_d/r_c)} \quad (5)$$

The relationship between r_d and r_c is easily explained in terms of a potential energy diagram as seen in Fig. 5. In this figure, the potential energy of an adsorbed oxygen molecule is plotted as a function of the molecule's distance from the solid surface. In Fig. 5, q_p represents the heat of physisorption and E_p the activation energy for transition from the physisorbed to the chemisorbed states. If we assume the ratio of the pre-exponential factors of r_d and r_c is K_1 then

$$r_d/r_c = K_1 \exp[-(q_p - E_p)/RT] \quad (6)$$

where R is the gas constant and T the absolute temperature. Equation (5) then becomes

$$S_0 = \frac{\alpha}{(1 + K_1 \exp[-(q_p - E_p)/RT])} \quad (7)$$

In all likelihood $\alpha \approx 1$ so that the quantity $(1+K_1 \exp[-(q_p - E_p)/RT])$ is equal to approximately 500 since $S \approx 2 \times 10^{-3}$. Therefore, to a good approximation,

$$S_0 = \frac{\alpha}{K_1} \exp[q_p - E_p/RT] \quad (8)$$

indicating that chemisorption occurs with an activation energy close to zero (i.e., $q_p > E_p$), a phenomenon found in the oxidation of many metals (9-11).

The result of this interpretation is that the residence time of a physisorbed oxygen molecule on the surface and its migration rate determine

the number of chemisorption sites accessible per physisorbed molecule and therefore the chemisorption rate. Hence, as the substrate temperature is increased, at fixed oxygen pressure and silicon incidence rate, the stoichiometry of the deposit will decrease as is observed in the reactive deposition of many oxides including reactively deposited SiO_x . This is due to the decrease in residence time of physisorbed oxygen mobility with increasing temperature.

(b) Oxide and Nitride Film Deposition

The new gas flow controller/argon ring set up at the target location was tested to determine P_{O_2} (max) before target oxidation occurs. The gas flow controller was found to be stable in the rf fields present but some small indication of oxygen contamination in the Ar line was suggested because of occasional peaks in reflected power readings. Si deposition rate tests were carried out both with and without (Ar released at the chamber wall ~ 6" from the target) the Ar ring. The without/with Ar ring data were 4.2/4.3 Å/sec at 300 watts (rf) and 6.2/5.8 Å/sec at 500 watts (with 3×10^{-6} torr base vacuum, 4 μm maintained Ar pressure and 4" source/substrate distance). The reflected power was generally steady in the 0-3.0 watt range except at 500 W, with the Ar ring, it jumped to 50 W. We thus concluded that O_2 was occasionally getting into the Ar line.

In order to work easily with 3" diameter wafers and to extend the substrate temperature range, considerable effort was expended in the development of a new substrate heater. Modifications to an existing two element quartz lamp were unsuccessful but the development of a carbon cloth heater was fairly successful. However, a deposited film was observed on the Si substrates placed on the heater during bakeout even with no

sputtering and no intentional gases present. Microprobe detected carbon and silicon in the film while EDAX analysis showed no obvious metals to be present. Based upon the partial success, a platinum wire heater was designed for the higher temperature work.

Relatively successful attempts have recently been made to deposit Si_3N_4 films even though our early work led to measured values of $n = 2.4$ to 2.8 instead of 2.03 . Using 250 W , $P_{\text{Ar}} = 4.0\text{ }\mu\text{m}$ and $P_{\text{N}_2} = 0.26\text{ }\mu\text{m}$, source to substrate distance was considered as the variable. At $5"$, no index could be measured which indicated a low density Si-rich film. At $3"$, the deposition rate was about 80 \AA/min and the film index ($\sim 1200\text{ \AA}$) was $n \approx 2.00$. At $4"$, an aluminum wire probe was inserted just above the substrate surface to provide a glow discharge during sputtering as an aid in dissociating the N_2 . In this case, a deposition rate of 90 \AA/min was found and the film index ($\sim 1500\text{ \AA}$) was $n = 2.09$. Thus, the use of the glow discharge was important since the deposition rate increased rather than decreased by $9/16$ in going from $3"$ to $4"$. From these experiments it was felt that nitride films from silicon oxy-nitride through Si_3N_4 to Si-rich nitrides could be easily deposited using these techniques and parameters.

2. Single Source Sputter Deposition of SiC Films

For high temperature operation ($T > 900^\circ\text{C}$), both the single quartz lamp heater and the double quartz lamp heater were found to be inadequate as a substrate heater because of shorting and arcing problems during operation. However, after considerable development effort a carbon-cloth heater was fabricated. To date, it has proven to be extremely stable in operation up to 900°C in a plasma environment. The present temperature

limitation is a matter of power supply capability rather than heater capability.

During this heater development study, a surface contamination problem was noticed. It was noticed on all depositions wherein an ion-gun surface cleaned substrate was used above $T = 600^{\circ}\text{C}$ and on substrates, not ion-gun cleaned, heated to $T = 900^{\circ}\text{C}$. In the latter case, a substantial surface conversion of the Si to SiC occurred ($\sim 2500 \text{ \AA}$ thick) as determined by x-rays and electron microprobe analysis. This SiC layer was non-uniform in thickness and triangularly shaped islands \sim several microns in size were observed. The source of the carbon was considered to be organic contamination in the chamber. Less contamination was observed after having scrubbed the chamber and the masking plus heater parts.

A Meissner trap was made from coiled stainless steel tubing and mounted on the inside of the chamber near the outer wall. Flowing liquid N_2 through the coil reduced the system pressure from typically 2×10^{-6} torr to 5×10^{-7} torr. Monitoring with the gas analyzer (RGA) showed that the trap primarily reduced the water vapor level in the chamber. This reduced the silicon surface conversion problem somewhat but not completely.

New Depositions

The list of new depositions are presented in Tables I and II. Surface conversion of Si to SiC was seen to an even greater degree at 900°C than with depositions at lower temperatures. A methanol rinse seems to make the depositions less crystalline, perhaps enhancing the surface conversion. Sample 564, with an HF dip surface clean and a 900°C SiC deposition without tin, appeared to be (via x-ray diffractometry) as high quality as our best earlier deposition (#82-233) although visually the film was not uniform.

No surface contamination was found with the deposition on sapphire. Via electron microprobe, tin was found in all the samples 597-601 (500°C to 800°C depositions) indicating that the tin target power of ~ 105 W was too high.

From Table II we note that a set of SiC depositions at 500 W was made on a variety of substrates. The thin film on (0001) sapphire is a great improvement over all previous depositions according to both the high x-ray count and a Read camera pattern which showed only the 111 β SiC reflection in a tight $\pm 3^\circ$ distribution about the substrate surface normal. Interestingly, this substrate had no ion gun cleaning prior to deposition. The sheet resistivity value for 82-124 was found to be quite low at $2.7 \Omega \text{ cm}$ compared to the highest ρ_s to date of $590 \Omega \text{ cm}$ (sample 81-124 on (1102) sapphire at 700°C). Sheet resistivity values for the depositions on oxidized Si were found to represent measurement of the substrate rather than the thin SiC film. Finally, the deposition on spinel could not support a voltage suggesting a serious interface problem. This film appears to be highly stressed and is gradually lifting off the substrate.

A number of SiC depositions that were examined by TEM showed a hexagonal α -SiC component not seen by any other analysis method and it was thought that this might arise from the extensive ion milling involved in sample preparation or from the electron beam. A number of very thin, $\sim 500 \text{ \AA}$, depositions of SiC on Si were made to sort this out (#619-623). No TEM analysis has yet been made but extensive optical microscopy at 1550 x indicated distinctive surface features in the micron size range. The largest features were triangular and appeared brighter in the microscope. Either tin or a different phase was suspected but tin was not detected via

dispersive x-ray analysis. These samples look interesting and may provide information about the early stages of growth of SiC on Si. A TEM sample preparation technique without using ion milling is underway.

3. Synthesis of Pd Silicide Films

<111> Si wafers were scribed and inserted in the sputtering chamber as described in the previous report (12). The wafer, which was located at the point where Pd_2Si was calculated to be deposited, was etched in dilute HF until the surface was hydrophilic and then the system was immediately sealed for pump down. Material was deposited at room temperature or at 400°C for 93 minutes to produce approximately 1 μm of Pd_2Si so that electron probe microanalysis could eventually be carried out on the film.

The results of the phase spread deposition, as determined by microprobe analysis, agreed within experimental error with the calculated results. The compositions shown in Table III were analyzed using x-ray diffraction. The Pd lattice was found to expand linearly at ~ 0.20% per atomic percent of added Si in the 1 to 10 At % Si range. At about 10% Si, amorphous material appears. This is expected because of the deep eutectic at ~ 15 At % Si. At ~20 At % Si, Pd_2Si is first observed and this phase increases in intensity until, at 27 At % Si, the material is entirely Pd_2Si . The material then transforms into PdSi at ~49 At % Si and it is unclear as to the exact progression of phases between Pd_2Si and PdSi as the Si increases.

Initially, when the samples had been freshly prepared, there were a great number of x-ray peaks found on the Si-rich side of Pd_2Si indicating both Pd_2Si and PdSi to be present. Later, more detailed analysis failed to detect any PdSi peaks until ~ 50 At % Si. Perhaps unusually high mobilities of Si in Pd_2Si near room temperature led to the indicated

structural rearrangement. X-ray analysis of the deposited films at the composition of Pd_2Si using a Read camera indicated strong texturing. The particular texture is that expected for Pd_2Si growth on (111) Si (Pd_2Si surface normal is approximately 9° from the Si surface normal).

For the elevated temperature ($400^\circ C$) phase spread deposition, where the entire substrate was located in the chamber at the position where Pd_2Si should form, the entire deposited film had the Pd_2Si structure although electron microprobe analysis showed $\sim 6\%$ variation. The larger region of reasonably homogeneous composition, as compared to the lower temperature phase spread deposition, was probably due to the increased surface mobility of Pd and Si.

4. Electrical Diagnostics of SiO_x Films

The designated goal of this research is to determine the feasibility of extracting useful and reliable data from non-contact in-situ monitoring of SiO_2 growth by the A.C. impedance technique. The proposed experimental set-up for such monitoring is as given in Fig. 6. Ideally, one would oxidize the Si samples at temperature T and, at periodic time intervals, one would perform an automated measurement from a desk top computer. An individual measurement would consist of various impedance readings ($B, G, X, R, \epsilon', \epsilon'', C_{p, p}$, etc.). When optimized, this measurement cycle should take ~ 1 min-30 min depending on the need for lower frequencies (1 mHz - 1 Hz). The result of this measurement cycle would be data on a floppy disc or magnetic tape to be eventually plotted as $X-R$, $B-G$ and $\epsilon'-\epsilon''$ plots. These plots would contain information on the combined impedance of the entire sample geometry. One would hope to isolate and extract the resistance, R_{ox} , and the capacitance, C_{ox} , of the bulk SiO_2 and

relate this to the thickness of the growing oxide, t_{ox} , via $R_{ox} = \rho(T)t_{ox}/A$ and/or $C_{ox} = \epsilon \epsilon_0 A/t_{ox}$. This process, with some on-line analysis of the data by the desk top computer, should yield real-time monitoring of the thickness without the need for plotting the non-impedance data.

The success of this experiment depends on the ability to view the plotted data ($X-R$, $B-G$, $\epsilon''-\epsilon'$) and sensitively distinguish one component of the electrical system from another. To perceive the problem, consider the sample electrical equivalent circuit given in Fig. 7. The dominant impedances will be the SiO_2/Si interface, the bulk SiO_2 and the air gap leading to the reduced equivalent circuit of Fig. 8.

Some preliminary C-V, I-V and AC measurements at room temperature showed that $C_i \sim C_{ox}$ at $25^\circ C$. Using conductivity data from Srivastava et al(13), we find that $\rho \sim 5 \times 10^{15}$ and $\rho \sim 10^{10}$ at $25^\circ C$ and $850^\circ C$ respectively so that $R_{ox} \sim 10^4 - 10^7 \Omega$ at $850^\circ C$ for $t_{ox} = 1000 \text{ \AA}$ and $A = 10 \text{ cm}^2 - 10^{-2} \text{ cm}^2$. Assuming that ϵ is independent of T , $C_{ox} \sim 3.5 \times 10^{-7} \text{ F}$ to $3.5 \times 10^{-10} \text{ F}$ (as A changes in this range).

The air gap brings in many complicated considerations. It must be wide enough to allow oxygen to diffuse freely to the oxide surface and yet it must be narrow enough to give a small value of C_{ag} and be experimentally controllable. If $A = 10 \text{ cm}^2$, $d = 1 \mu\text{m} \rightarrow C_{ag} \sim 10^{-10} \text{ F}$ but if $d = 10^{-6} \text{ cm} \rightarrow C_{ag} \sim 10^{-8} \text{ F}$. Since we now have some idea of the parameter magnitudes in Fig. 8, we can now synthesize the sample plots $X-R$, $B-G$ and $\epsilon''-\epsilon'$ if we neglect C_i . The $X-R$ plots illustrate the salient features present in all the plots so we shall consider only these. In Figs. 9(a) and 9(b), we note the great difference in the X versus R plots as C_{ag} is increased from 10^{-10} F to 10^{-8} F . In the former case, it is not clear that we can readily

separate the effects of the two components. From this shape of curve we can conclude that C_{ag} is of the same order as C_{ox} otherwise such a strong coupling would not have occurred. In Fig. 9(b), the two segments of the circuit are uncoupled and we can readily distinguish C_{ag} from C_{ox} .

From the foregoing, we can conclude that the effect of an arbitrary interface impedance will be generally much easier to pick out of the data base when the two initial impedance effects are "displayed" at sufficiently different frequency ranges. This is not true when $C_{ag} = 10^{-10} F$ which is the experimentally more realizable value. Thus, we must conclude that the use of this technique for sensitively studying unknown systems is only on the edge of experimental viability for the general case. For specific situations when one can arrange C_{ag} to be very different from C_{ox} , the technique will have great utility for studying interface effects.

B. Theoretical Results

1. Film Formation Modeling via Computer Simulation

a. Parametric Investigations

Details of film formation require a knowledge of the map of stored strain energy in the substrate-film combination. However, the available techniques for evaluating the stress tensor components and the elastic constants of a two phase system in the immediate vicinity of the interface region are quite inadequate so we decided to develop a generalized statistical thermodynamic approach to the problem. The first result is that individual stress and elastic formula have been developed for the interface layers by calculating the "local" pressure variations across the interface. The basic results for the stress, σ_{ij} , and elastic constants C_{ijkl} , are

$$\sigma_{ij} = \frac{1}{V} \frac{\partial A}{\partial \epsilon_{ij}} \quad (9)$$

and

$$c_{ijkl} = \frac{1}{V} \frac{\partial^2 A}{\partial \epsilon_{ij} \partial \epsilon_{kl}} \quad (10)$$

where

$$A = -kT \ln Q \quad (11)$$

and

$$Q = \frac{1}{N!h^{3N}} \int \dots \int dx_N^N d\rho^N \exp[-H(x^N, \rho^N)/kT] \quad (12)$$

Here, A is the Helmholtz free energy, ϵ_{ij} is the Lagrangian strain parameter and H is the Hamiltonian for the system. Equations (9) and (10) are always evaluated at zero strain but more general forms have been derived in the vicinity of zero strain. Explicit analytical forms have been calculated for the strain derivatives using both two-body (Lennard-Jones) and three-body (Axelrod-Teller) potential energy functions. From this work we find that (i) the entire variation from one stress component or elastic constant to another is determined by the general symmetry of the two and three particle distribution functions so that the result can be separated into a geometrical combination factor and a material combination factor, (ii) new and unique symmetry patterns are introduced via the three-body potential so that, in principle, all 21 elastic constants can be unique (rather than just 15 for the purely two-body PEF case) and (iii) our equations are perfectly general and apply to both bulk solid as well as

non-homogeneous regions like interfaces.

As mentioned in the previous report⁽¹²⁾, the adlayer-substrate interaction effects are being investigated using a system of 1000 particles (~ 400 adlayer, X, and ~ 600 substrate, Ag(111)) using only two-body forces for a silver substrate and adlayers of Cu(111), Au(111), Ni(100 and Ag(111)). The bottom three layers of the six substrate layers are held fixed and all thermodynamic quantities were calculated considering only the "core" region of the hexagonal slab (to eliminate edge effects). The calculations generated potential energy profiles, density profiles, radial distribution function, virial profiles, vibrational spectra and stress components. Because of its differential character the virial reflects the mismatch of the sites at the interface⁽¹²⁾; however, some of the stress components give the most interesting results.

In spite of the 11.5% mismatch in the Cu/Ag system, the interface is coherent with increased compressive forces in the substrate parallel to the interface while the adlayer itself is in the tensile state. For σ_{xx} (lying in the interface), only the top Cu layer shows a stress dipole behavior while, for σ_{zz} (perpendicular to the interface) a much larger dipole effect exists for the first layer with a smaller dipole effect existing for the lower layers and, with σ_{xy} (in-plane shear stress), no stress dipole effect exists at all. The results for σ_{xx} and σ_{zz} are given in Fig. 10.

For the Au/Ag case, although the atomic mismatch is only 0.1%, a very strong stress effect is observed because the Au-Au interaction energy is much stronger than the Au-Ag interaction energy. The vibrational frequency spectra for the Ag atoms at the Au/Ag and Cu/Ag interfaces also displayed considerable differences in peak positions and shapes. The largest effect

was found for the z-component of the vibrational spectra due to the heavy mass of the Au atoms.

For the Ni/Ag case, the interface exhibits a structural channel direction with a very different stress picture along versus normal to the channel direction. Along the channel direction there is no strong coupling of atomic positions across the interface so there is negligible stress coupling, however, perpendicular to the channel direction, strong correlation of atomic positions and strong stress coupling exists. This is demonstrated in the comparison of σ_{xx} and σ_{yy} presented in Fig. 11.

We find that our method of resolving the stress contributions by atomic layers is a workable technique with real merit because the calculated results can be understood in terms of atomic processes. It looks as if (i) the stress dipole effect may be useful as a yardstick for measuring the surface influence penetration into the bulk, (ii) the cross-interaction parameters (ϵ_{x-Ag}) is an important guide to anticipate tangential shear strain dependence and (iii) stress effects, in the absence of atomic mismatch, may provide information on clustering tendencies and process activation barriers. Extension of this work to include three-body forces and periodic boundary conditions seems to be an important step to take.

(b) Simulation of Systems with Si and O Atoms

A Monte-Carlo procedure, based on two- and three-body potentials was employed to simulate crystalline α -cristobalite and α -quartz structures at $T = 50^{\circ}\text{K}$ and $T = 300^{\circ}\text{K}$. Iterations were carried out beyond the complete equilibration stage (monitored by variation of the total energy). Both the radial distribution function (RDF) and the angular

distribution function (ADF) for Si-O-Si and O-Si-O are determined and are shown in Figs. 12 and 13 for α -cristobalite at 300°K. Analysis of these results indicates that the initial crystalline structures for both phases are quite stable implying that the potential energy parameters used in these computations provide deep and stable minima at the temperatures considered. No changes are found in the RDF and ADF when the number of atoms was increased from 96 to 216. The data of Fig. 14 for Si-O-Si angle peaks at $\sim 155^\circ$ which is a little high compared to the experimental data.

At $T > 2000^\circ\text{K}$, both the α -quartz and the α -cristobalite displayed liquid-like characteristics in the RDF's as expected. This is an important result because the Born-Mayer-Huggins PEF used by almost all other investigators for SiO_2 requires them to go to $T \sim 5000^\circ\text{K}$ before liquid-like characteristics appear.

Two isolated clusters, SiO_4 and Si_2O_7 , were treated separately with the Monte-Carlo procedure at $T = 300^\circ\text{K}$. Iterations of long duration indicated that clusters initially generated as tetrahedral units preserved their tetrahedral structure.

We next attempted to simulate the condition of the SiO_2 surface using the Monte-Carlo technique. Figure 14(a) shows an unrelaxed (100) surface of α -cristobalite while Fig. 14(b) shows the reconstructed surface condition. In this computation, the top four layers of the system were allowed to relax while the remainder of the lattice was held fixed. Periodic boundary conditions were used on our basic system of 72 Si and 144 O atoms (3x3x3x12 atoms/unit cell). Comparing Figs. 14(a) and (b), we note that oxygen atoms of the first layer tend to form pairs with some regularity while O atoms of the third layer do not move. These pairs appear to be in some sense correlated. We have not confirmed any long

range regularity but three canonical configurations have been noted: (i) oxygen pairs on alternate sites forming a connected structure between adjacent rows, (ii) two oxygen pairs in parallel on adjacent sites and (iii) two oxygen pairs in series along the directional SiO_2 bond.

REFERENCES

1. W.A. Tiller, "Fabrication and Properties of Multilayer Structures", Final Report on DARPA Contract MDA903-79-C-0484 for period September 1, 1979 to August 31, 1981.
2. H. Ibach, K. Horn, R. Dorn and H. Luth, *Surface Science* 38, 433 (1973).
3. R. Dorn, H. Luth and H. Ibach, *Surface Science* 42, 583 (1974).
5. J.N. Miller, I. Lindau and W.E. Spicer, *Phil Mag. B* 43, 273 (1981).
6. E. Ritter, *J. Vac. Sci. Technol.* 3, 225 (1966).
7. Garfolini, T. Halicioglu, and G.M. Pound, *J. Non-Cryst. Solids* 37, 411 (1980).
9. E.F. Idzak, *Opt. Spec. (USSR)* 15, 54 (1963).
10. C.A. Neugebauer and R.A. Ekvall, *J. Appl. Phys.* 35, 547 (1964).
11. C.A. Neubauer and J.R. Randen, *Proc. IEEE* 52, 1234 (1964).
12. W.A. Tiller, "Fabrication and Properties of Multilayer Structures," First Semiannual Report, 1 September 1981 - 28 February 1982.
13. J.K. Srivastava, M. Prosad and J.B. Wagner, Jr., "Electrical Conductivity of Silica Thermally Grown on Silicon," to be presented at the Washington Electrochemical Society Meeting, October 1983.

TABLE I
SiC Sputter Depositions

Number	Substrate	Clean*	T, SiC, Sn	Purpose
563	111 Si	as rec'd	900°C, 600W, ϕ	heater cycle + dep
564	"	Hf, DI	" "	dep
572	"	as rec'd	25°C, ϕ , unstable	Sn rate test
573	"	MeOH, DI	25°C, ϕ , 180W	"
		"	108W	"
		"	44W	"
574	"	MeOH, DI	25°C, 600W, ϕ	SiC rate test
574.5	"	A, HF, MeOH, DI	900°C, ϕ , ϕ	heater cycle
575	"	"	900°C, 600W, 166W	dep with Sn
576	ITO2 A/ Al_2O_3	A, DI	" " 156W	" on sapphire
596	111 Si	C, DI	" ϕ ϕ	heater cycle, cal
597	"	"	500°C, 600W, 110W	new T
598	"	"	600°C, 600W, 108W	"
599	"	"	700°C, 600W, 101W	"
600	"	"	800°C, 600W, 104W	"
601	"	"	" " 96W	new Sn

* DI rinse implied between each step; A is a boil in $\text{H}_2\text{O}_2/\text{NH}_4\text{OH}$ and C is the $\text{H}_2\text{O}_2/\text{H}_2\text{SO}_4$ boil.

TABLE II
SiC Sputter Depositions

A. 600 W, 2" system, 6 1/2" source-substrate.

Number	Substrate	T	Tin Power	Feature Size (μm)
82-617	(111)Si	900°C	Heater Cycle	3.5-4.0
82-619	"	750°C	-	0.6-1.2
82-620	"	750°C	20 W	0.6-1.2, 1.3-2.3
82-621	"	750°C	50 W	1.0-2.6
82-622	"	900°C	20 W	1.0-2.0, 1.3-3.8, 4.2-6.5
82-623	"	900°C	50 W	0.6-1.3, 1.3-3.2, 3.2-4.5

B. 500 W, 3" system, 3" source-substrate

Number	Substrate	T	Relative X-ray Peak Height	Reflections in Read Pattern
82-123	$\text{O}_x(100)\text{Si}$	900°C	0.4	111, 220, 222
84-124	(0001) Al_2O_3	800°C	100.0	111
82-125	$\text{MgO Al}_2\text{O}_3$	800°C	3.6	111, 200, 220, 222, 1010
81-233*	(111)Si	750°C	11.5	111

* Best previous deposition

TABLE III

Pd-Si Phase Spread DepositionSi power = 570 W RF \rightarrow 272 $\text{\AA}/\text{min}$; $P_{\text{Ar}} = 3 \mu\text{m}$ Pd current = 0.11 A \rightarrow 200 $\text{\AA}/\text{min}$; $t = 93 \text{ min}$

<u>Composition</u>		<u>Structure</u>
At % Si	At % Pd	
0	100	
2	98	
4	96	Pd
6	94	
8	92	
10	90	
14	86	Amorphous & Pd
17	83	Amorphous
19	81	"
23	77	Amorphous & Pd_2Si
33	67	Pd_2Si
36	64	
41	59	Pd_2Si & PdSi
44	56	
52	48	PdSi
66	34	?
76	24	?

FIGURE CAPTIONS

1. Oxygen concentration for reactively synthesized films is shown as a function of the ratio of the oxygen (O_2) and silicon incidence rates for Type IIA and IIB experiments and for the thermal source results of Ritter⁽⁶⁾.
2. Oxygen concentration (x in SiO_x) is shown as a function of dynamic exposure, L_D , for films deposited using the Type IIA and IIB experimental arrangements and the thermal data of Ritter⁽⁶⁾.
3. Experimental results for Type IIA (I) and Type IIB (●, ■, ▲) are compared to the reported results of oxygen coverage on Si(111) surfaces as determined by HRES (□) ellipsometry (○) and Auger analysis (△) assuming that dynamic exposure (L_D) and exposure (L) are equivalent.
4. X in SiO_x is shown as a linear function of dynamic exposure, L_D , (Torr-sec) allowing estimation of the sticking coefficients, S , for oxygen in the Type IIA and Type IIB experiments (see Eq. (1)).
5. The intramolecular potential, V_p , is plotted versus distance illustrating the potential wells for both chemisorption and physisorption is schematically shown. The physisorbed state (DEF) represents the mobile precursor with an adsorption energy q_p . If the activation energy, E_p , for transition from the precursor to the chemisorbed state (ABC) is less than q_p , the activation energy for chemisorption is zero.
6. Schematic illustration of experimental set-up for non-contact, in-situ monitoring.
7. Sample electrical equivalent circuit for Fig. 6.

8. Reduced equivalent circuit for Fig. 6.
9. Plots of circuit reactance, x , versus circuit resistance, R , with $C_{ox} = 5 \times 10^{-11} F$ and $R_{ox} = 2 \times 10^5 \Omega$ at a range of frequencies for the two cases (a) $C_{ag} = 10^{-10} F$ and (b) $C_{ag} = 10^{-8} F$.
10. Stress components σ_{xx} and σ_{zz} for the Cu (111) adlayer/Ag (111) substrate system as a function of atomic position normal to the interface.
11. Stress components σ_{xx} and σ_{zz} for the Ni (100) adlayer/Ag (111) substrate system as a function of atomic position normal to the interface.
12. Radial Distribution Function for α -cristobalite (300°K) as a function of bond length: (a) Si-Si bonds, (b) O-O bonds, (c) Si-O bonds, (d) total bonds.
13. Angular Distribution Function for α -cristobalite (300°K) as a function of angle for both Si-O-Si and O-Si-O.
14. (100) Surface of α -cristobalite
(a) before relaxation
(b) after relaxation.

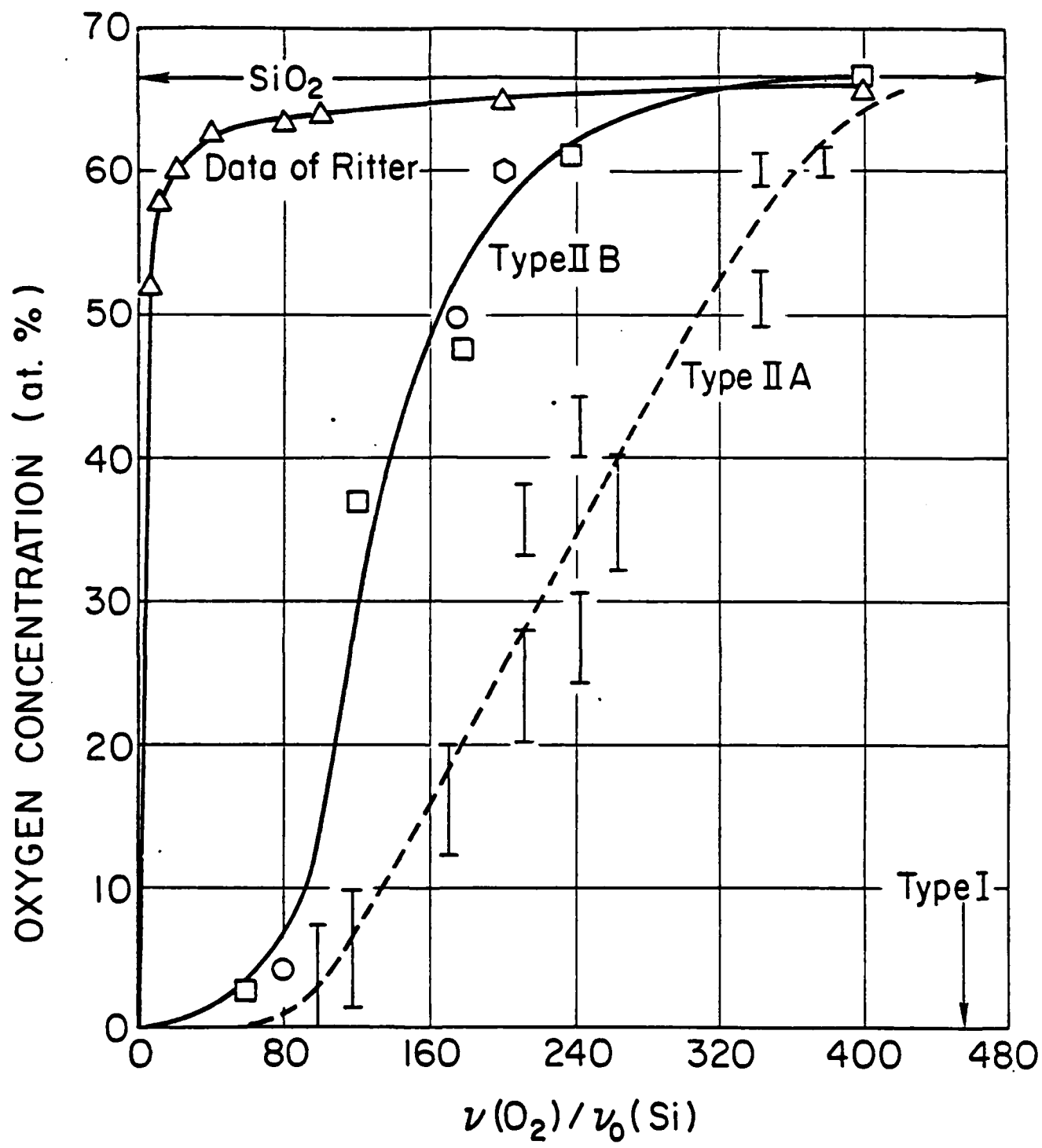


FIGURE 1

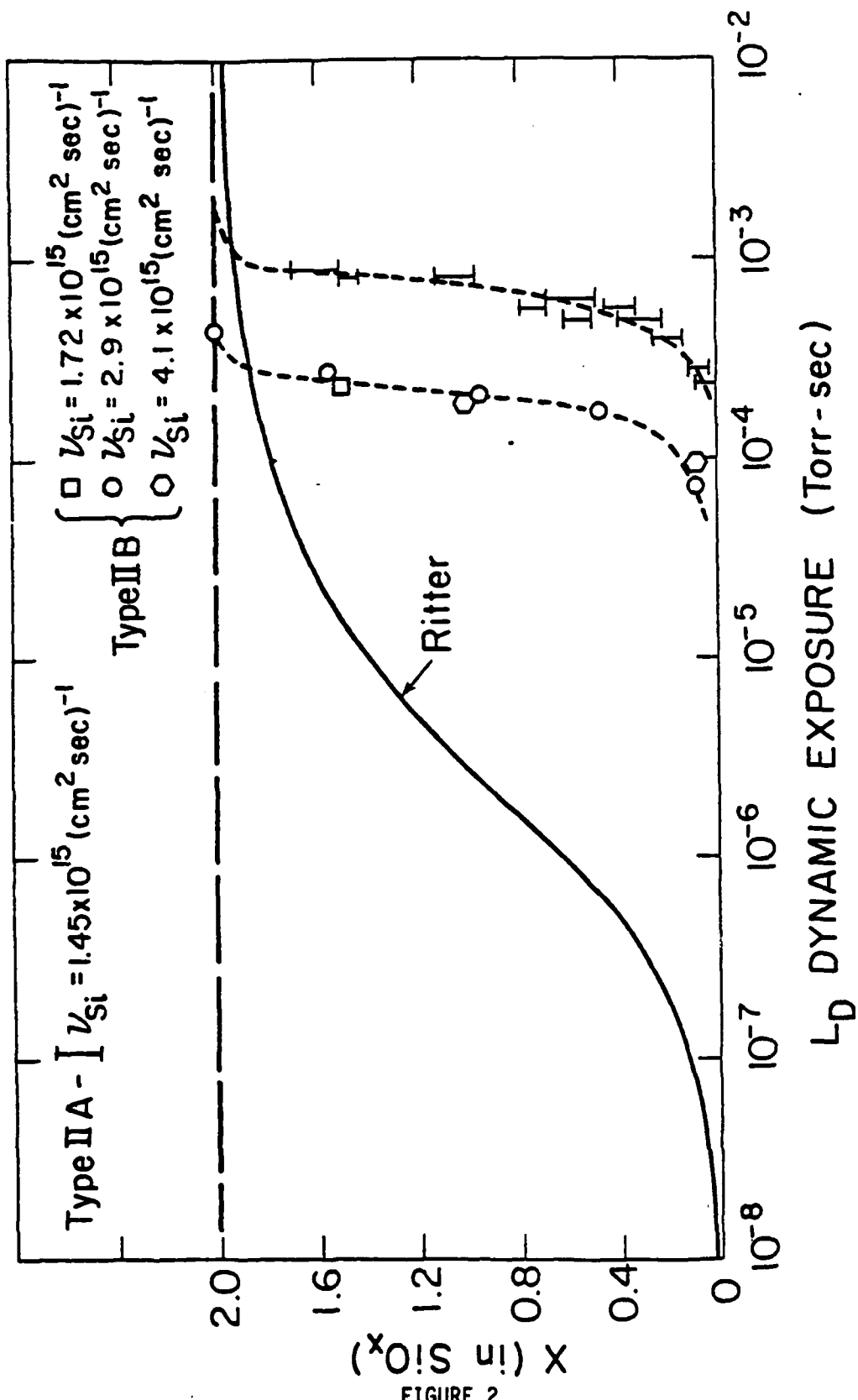


FIGURE 2

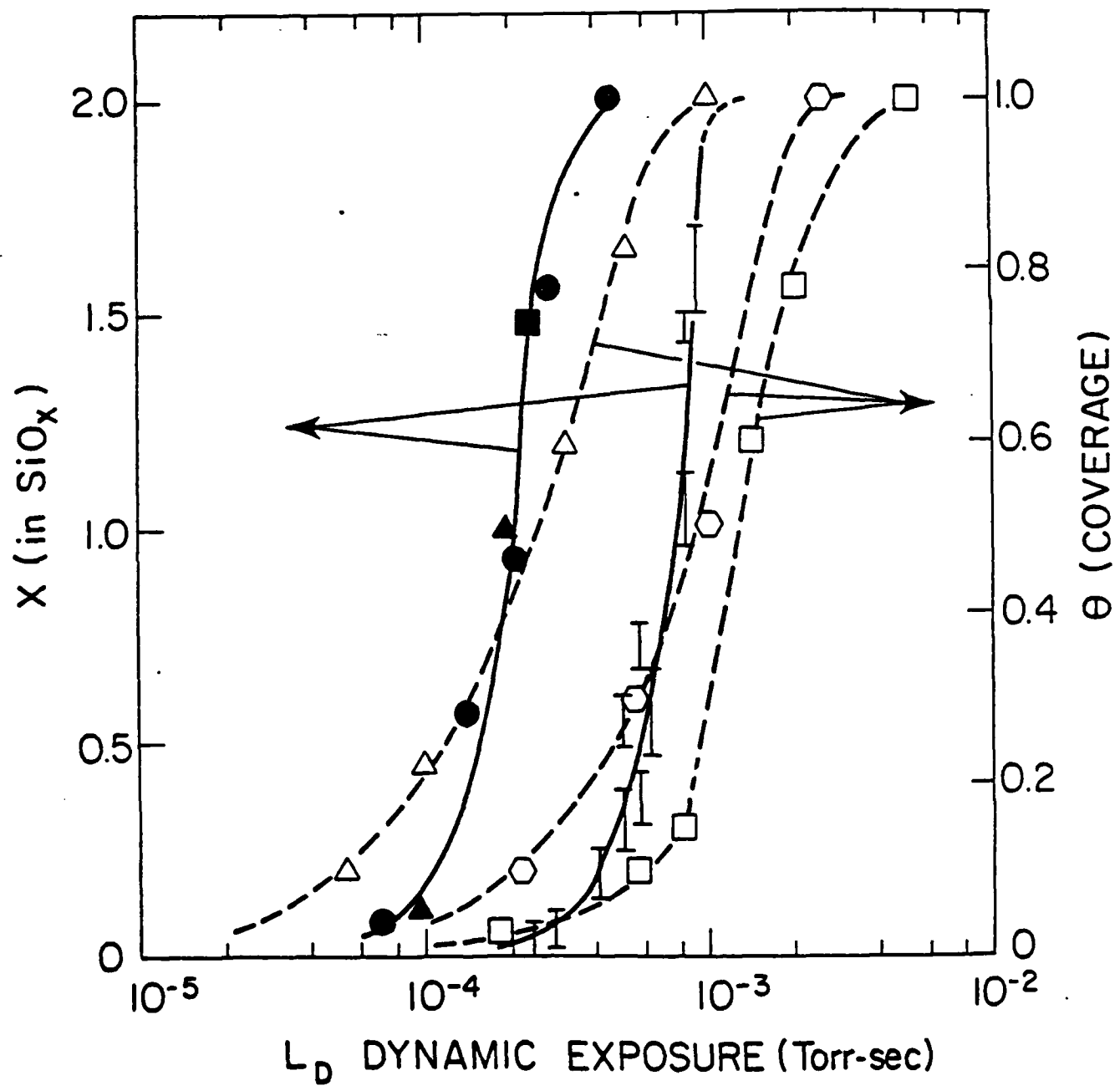


FIGURE 3

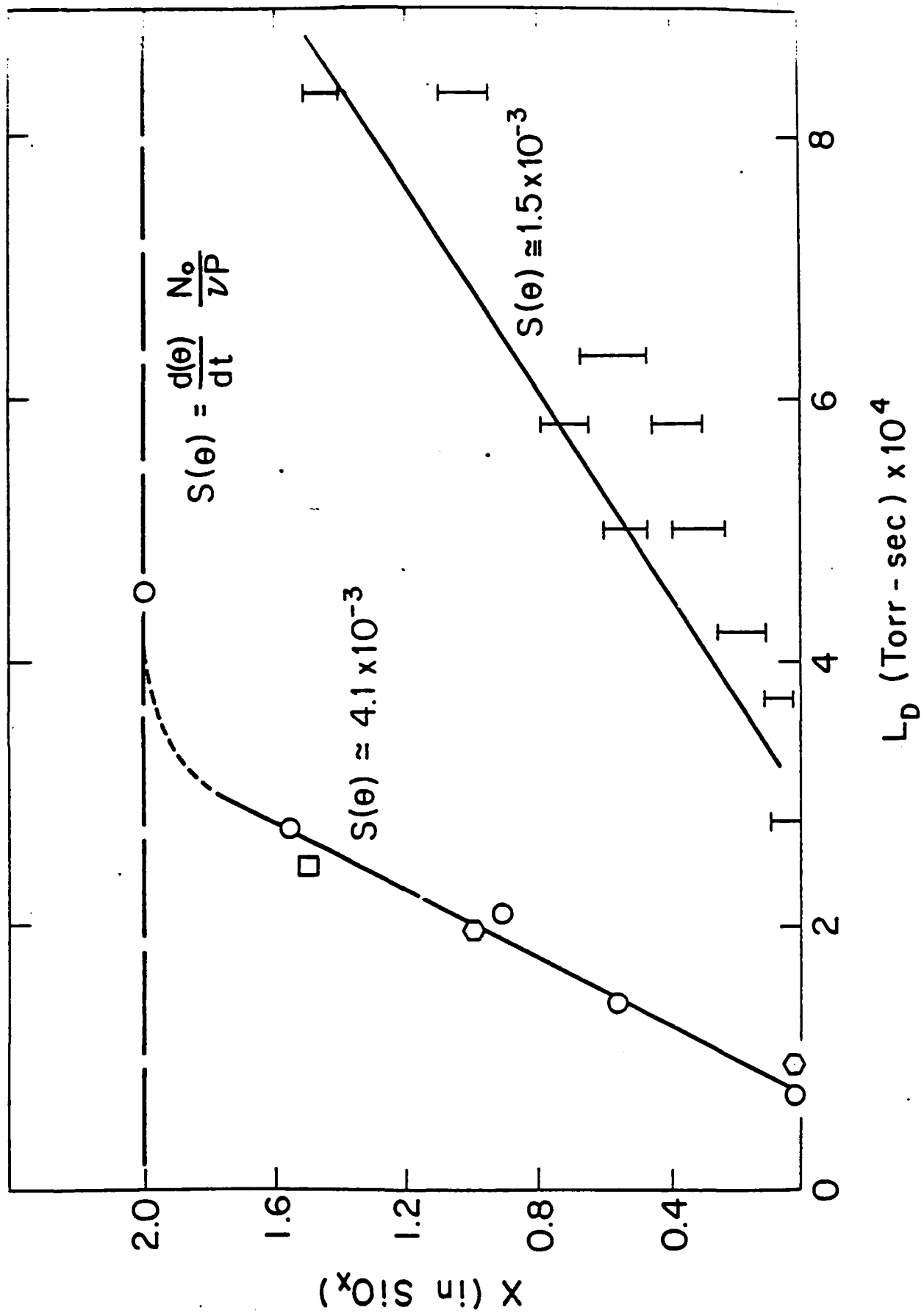
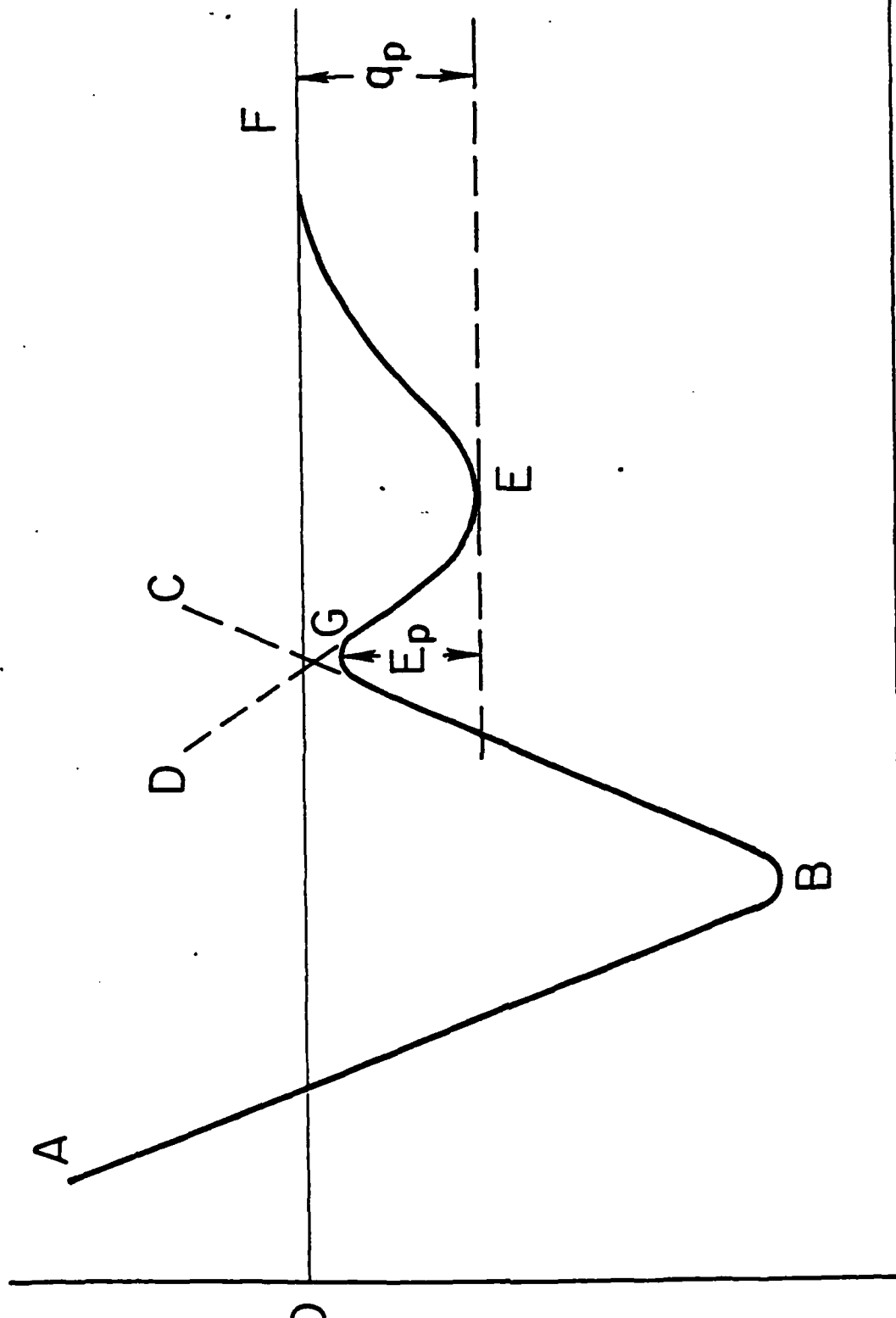


FIGURE 4



Potential Energy

FIGURE 5

Adatom - Surface Atom Distance

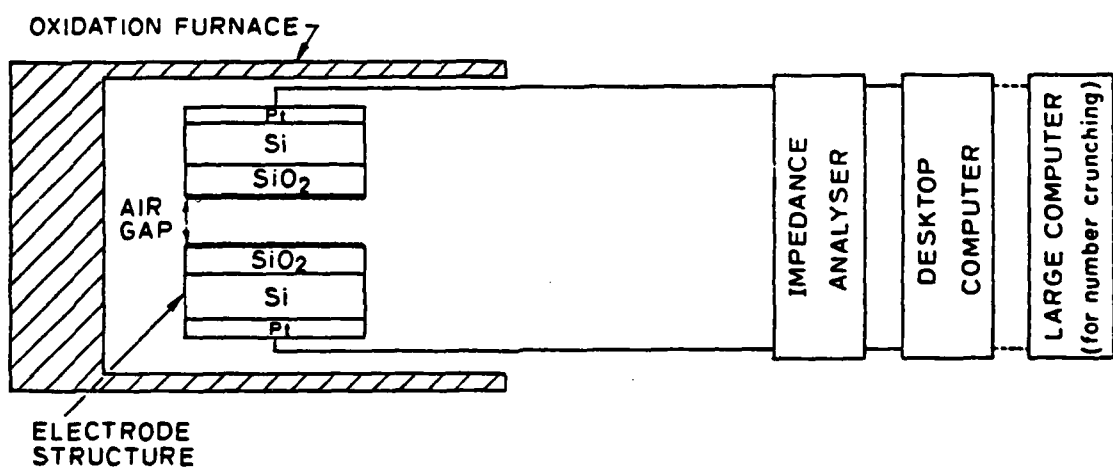


FIGURE 6

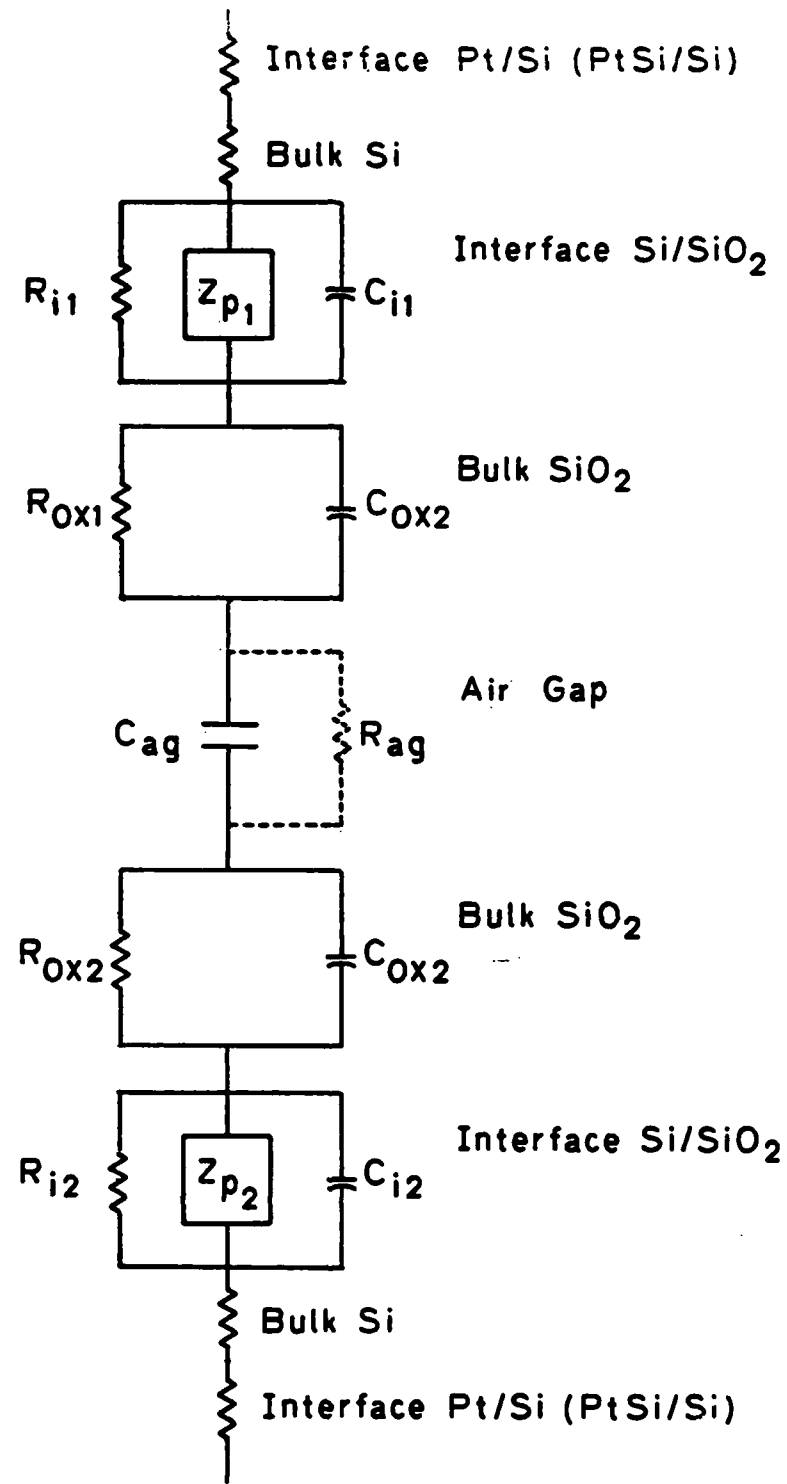


FIGURE 7

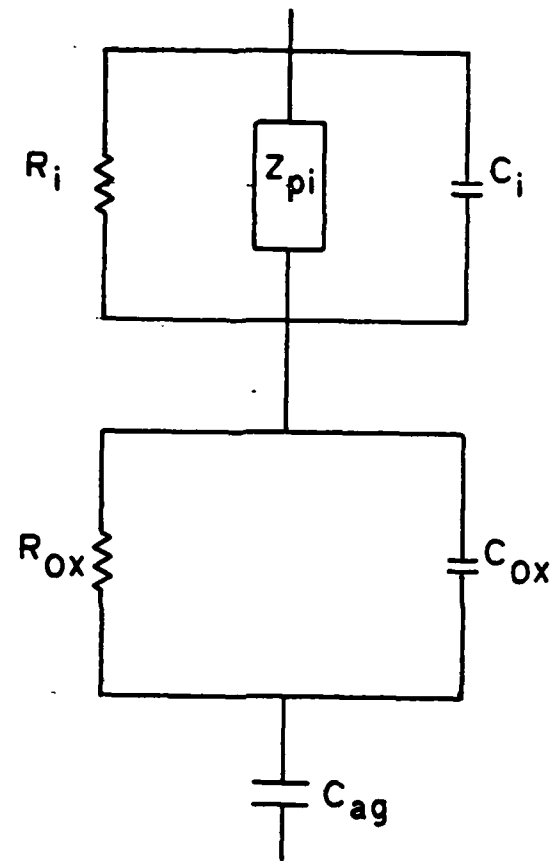


FIGURE 8

Ce11 Simulation Cag=E-10, T=850C

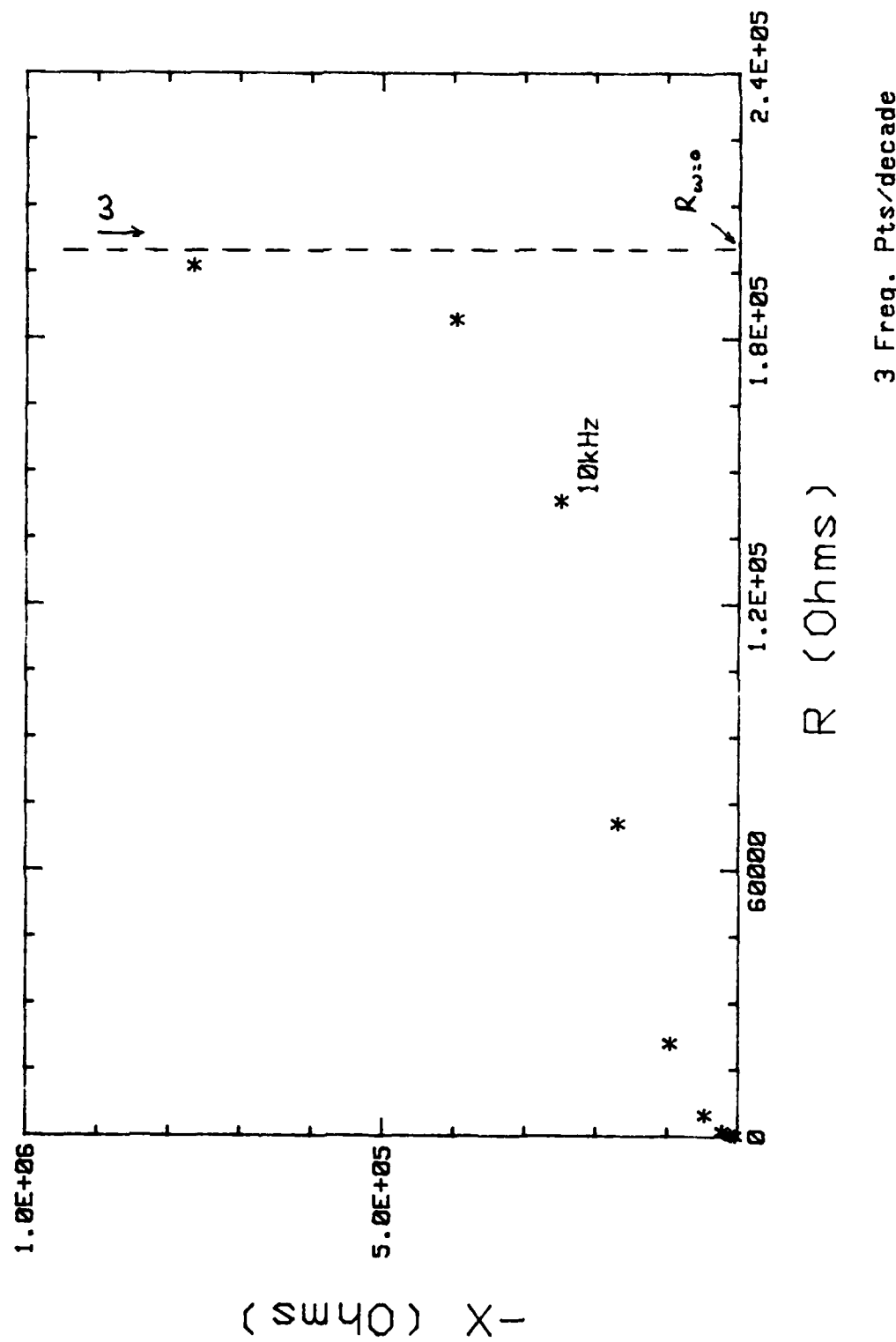
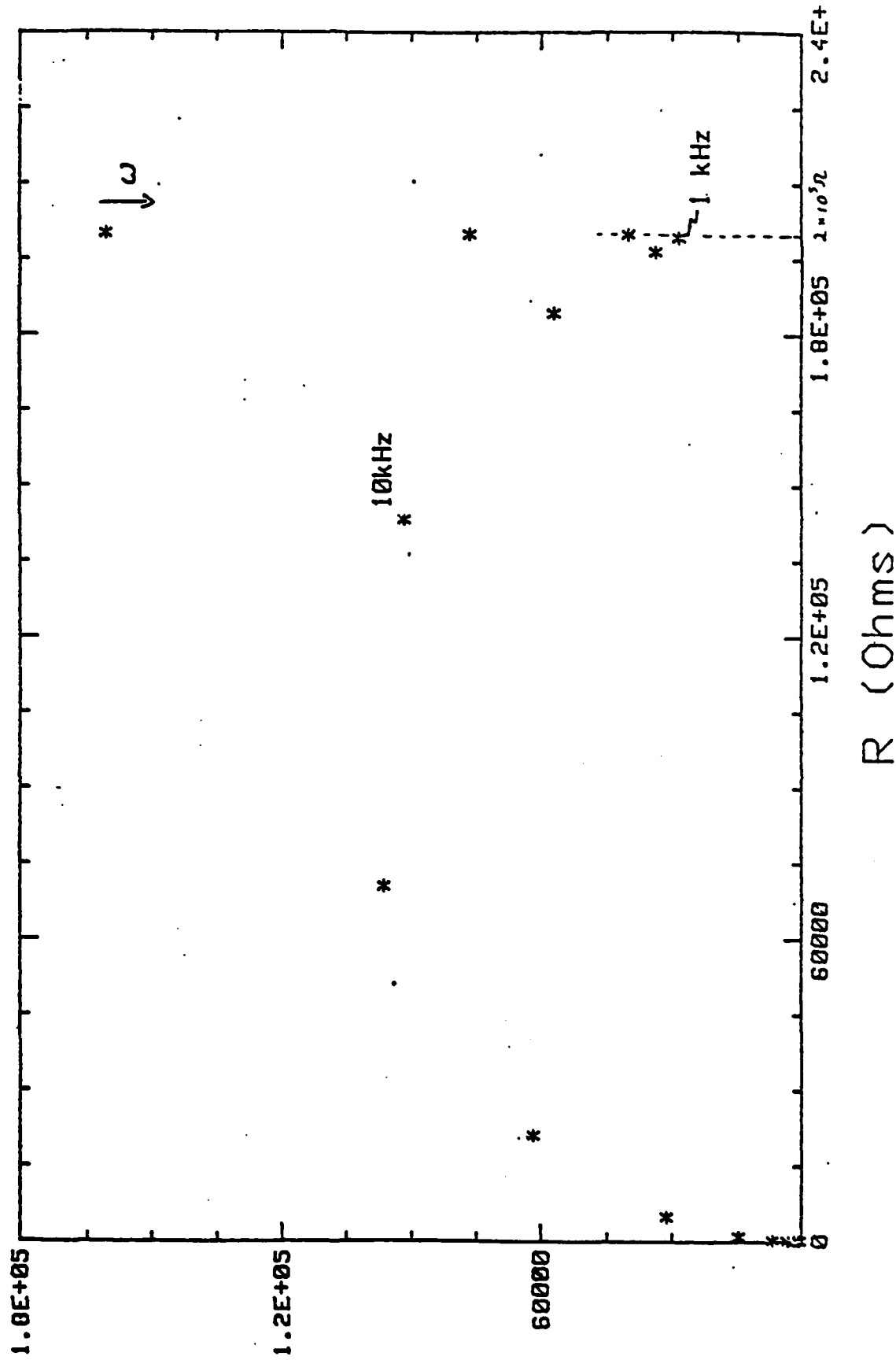


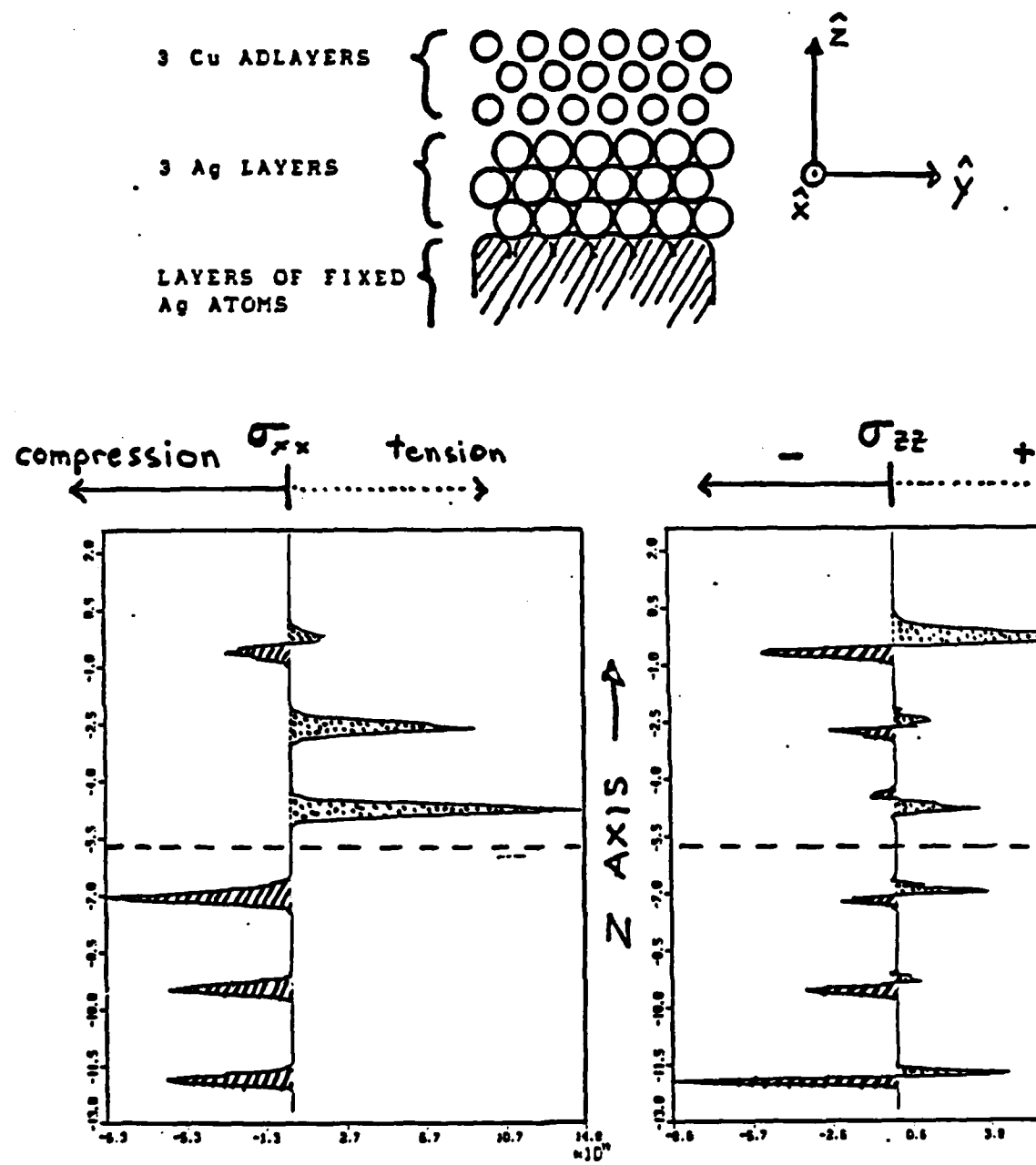
FIGURE 9a

Cell 1 Simulation $C_{ag}=E-8$, $T=850C$



(SW40) X -

FIGURE 9b



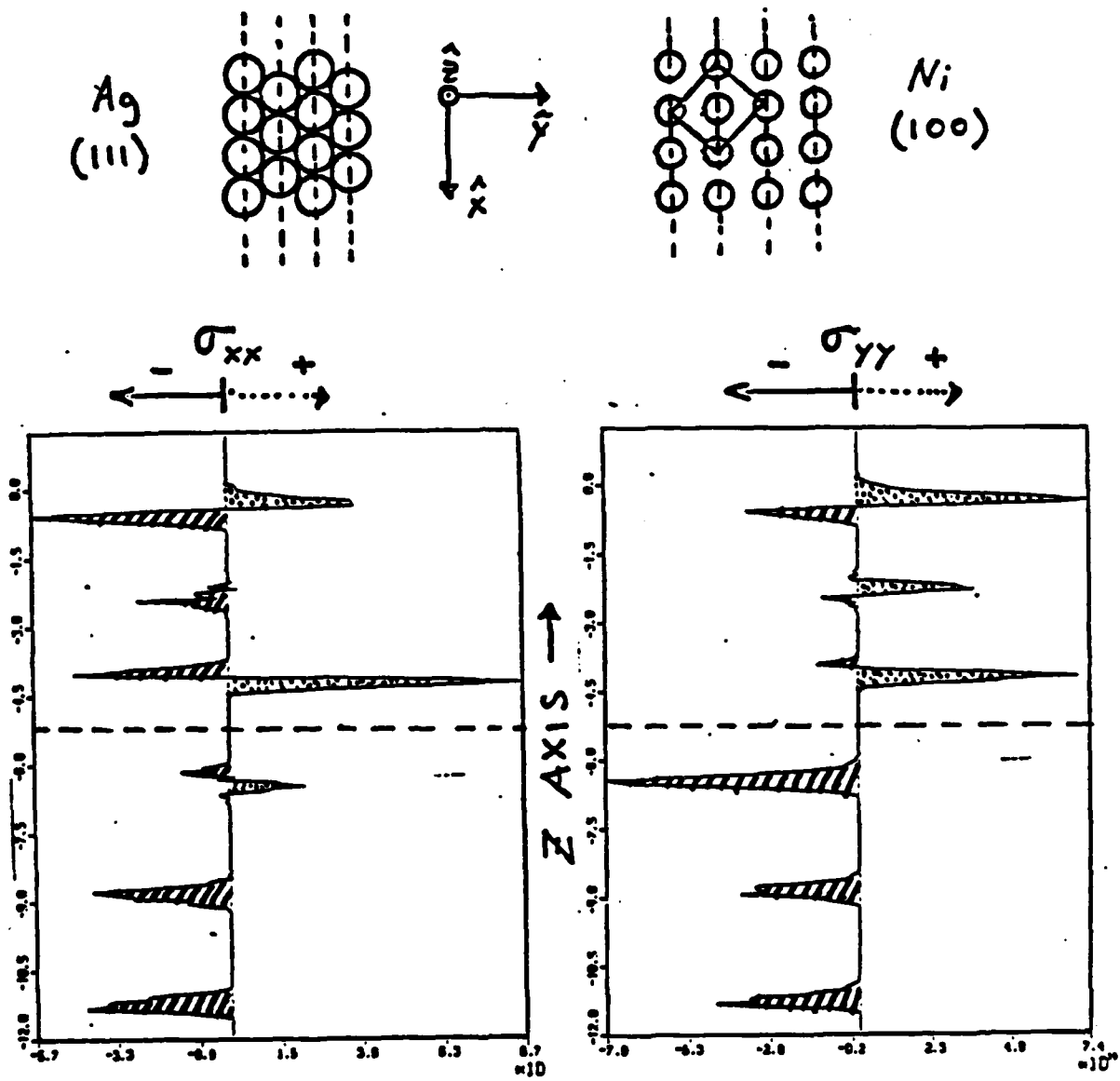


FIGURE 11

RADIAL DISTRIBUTION BOND LENGTH

SI-SI BOND

ALPHA CRYSTOBALITE
T= 300K

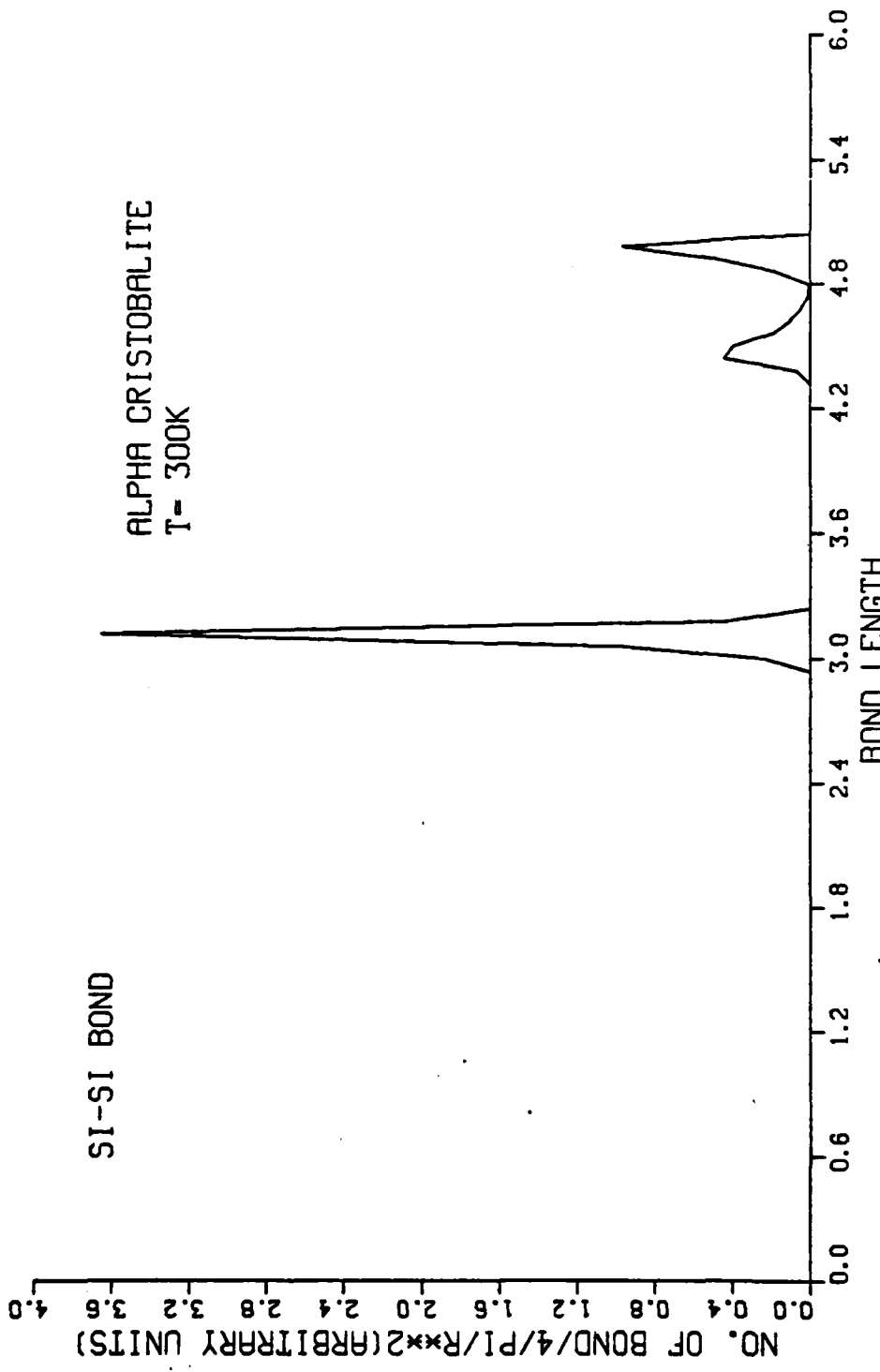


FIGURE 12a

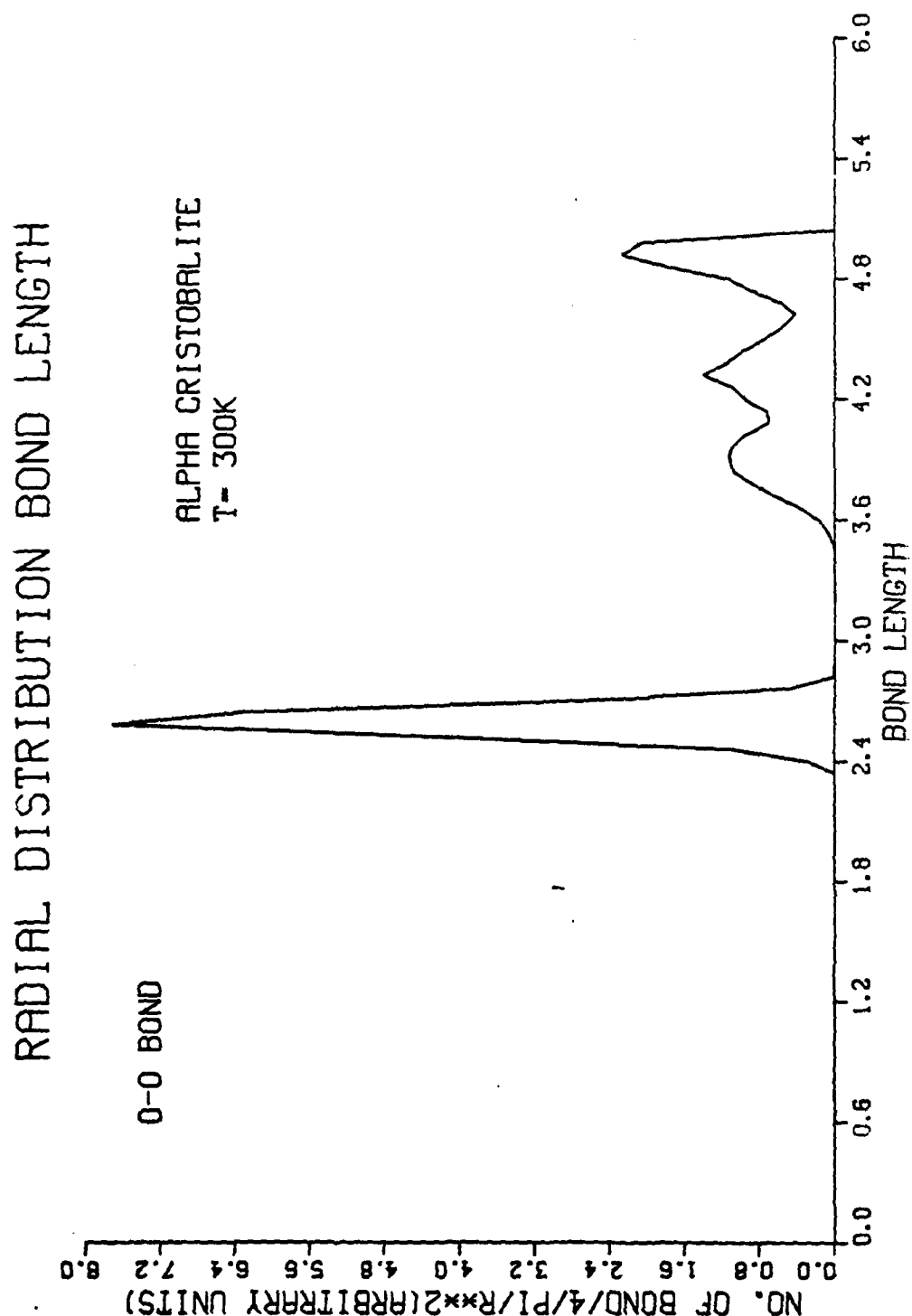


FIGURE 12b

RADIAL DISTRIBUTION BOND LENGTH

SI-O BOND
ALPHA CRYSTOBALITE
T= 300K

NO. OF BOND/4/PI/R²(ARBITRARY UNITS)

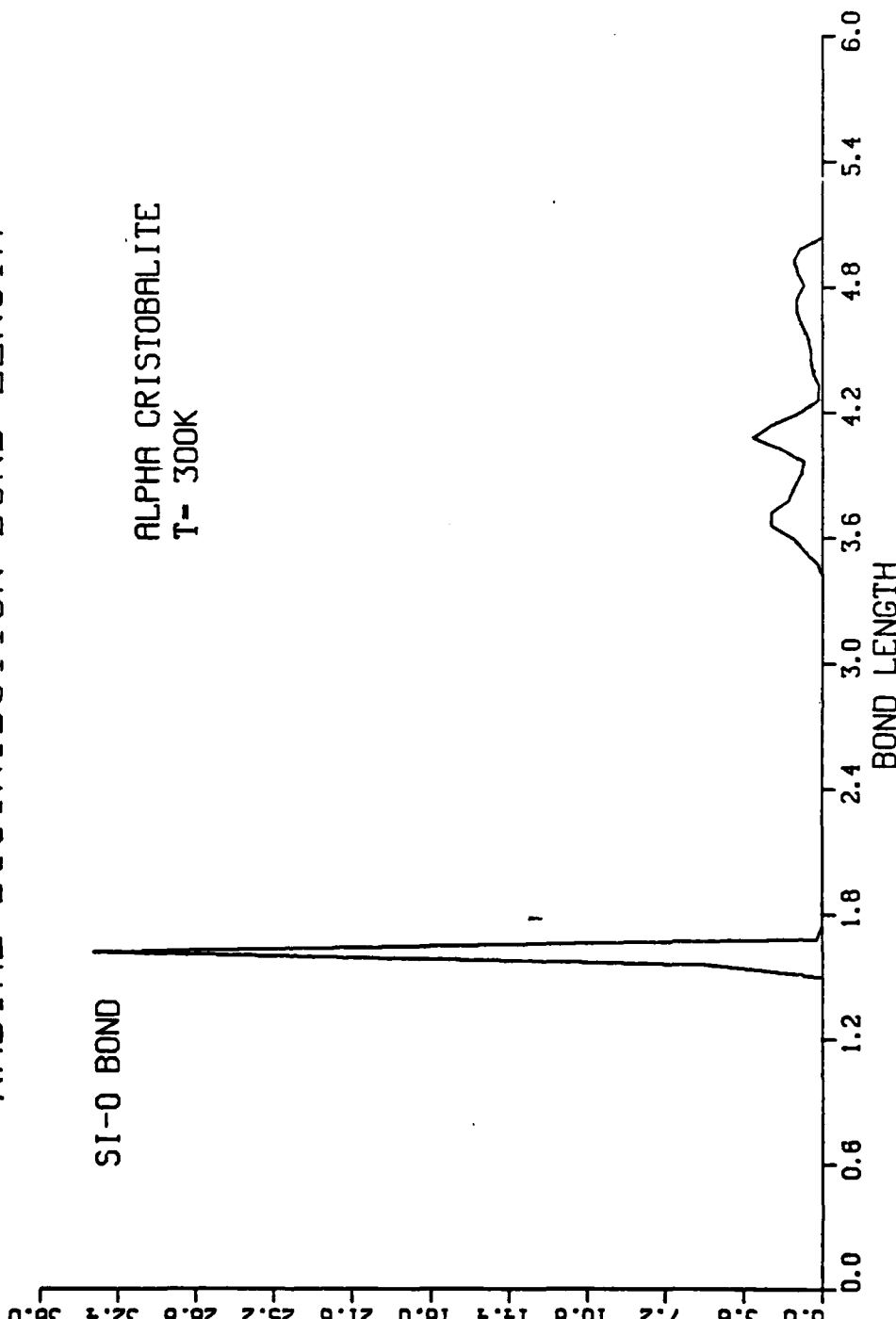


FIGURE 12c

RADIAL DISTRIBUTION BOND LENGTH

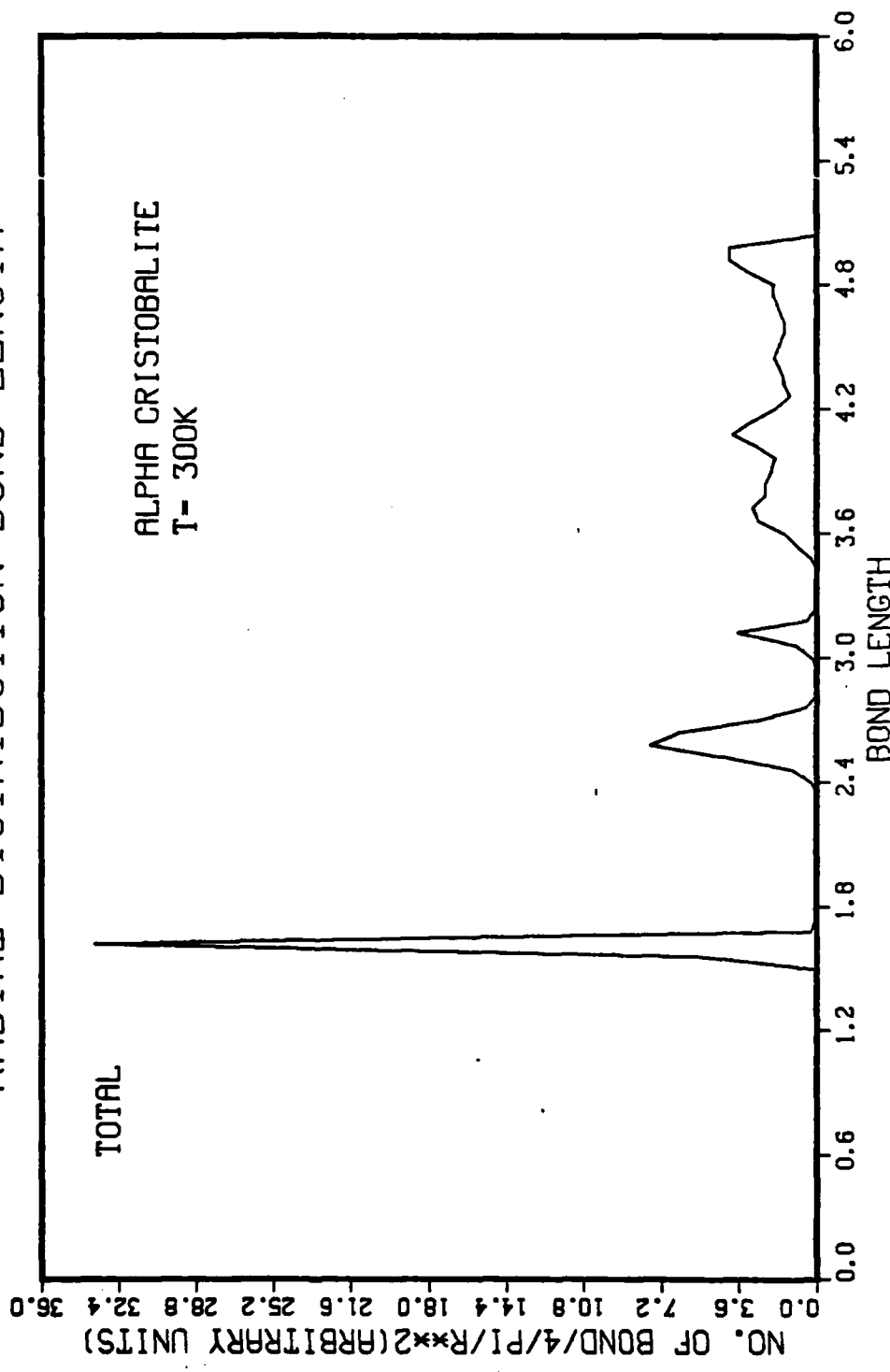


FIGURE 12d

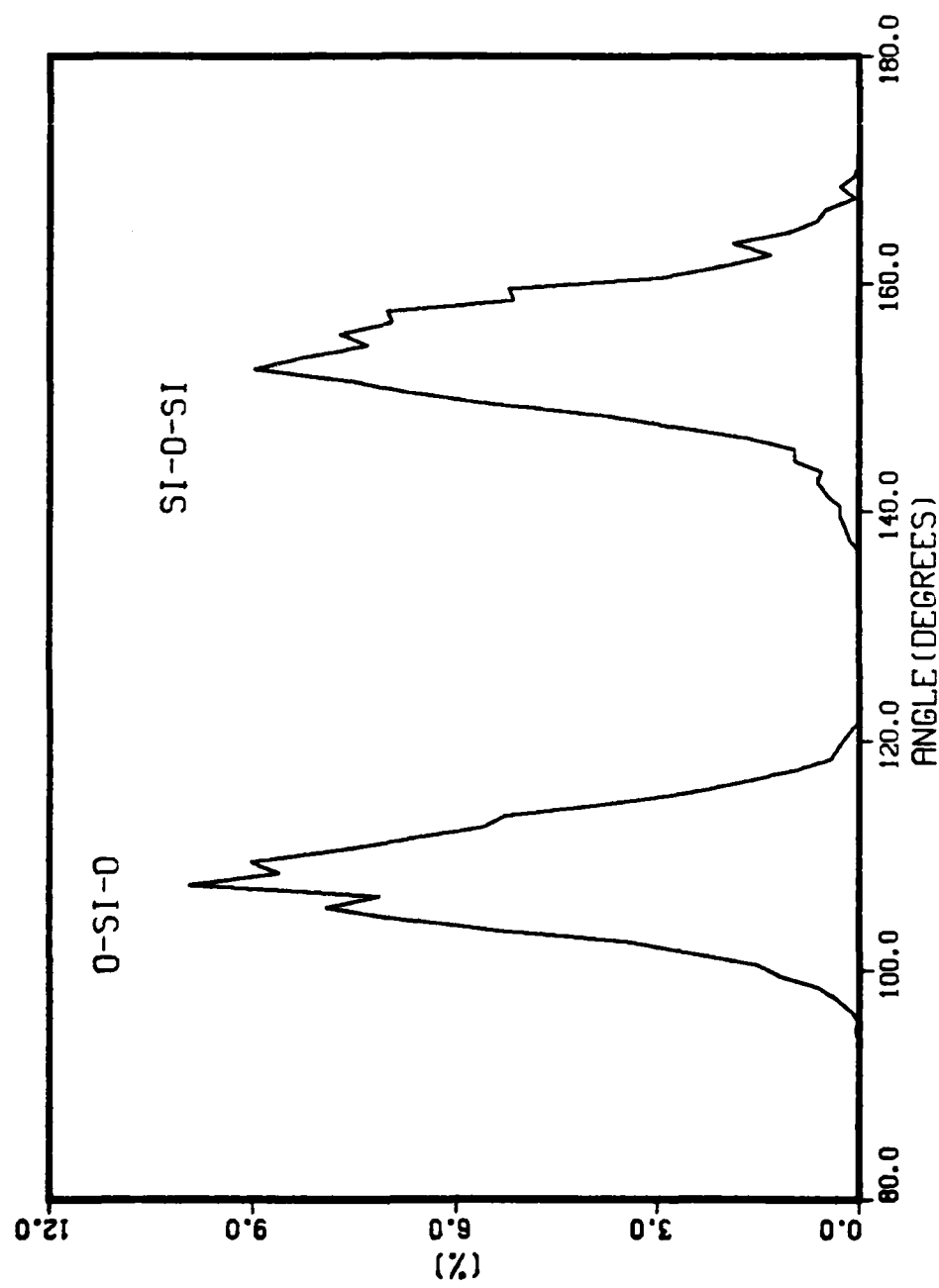


FIGURE 13

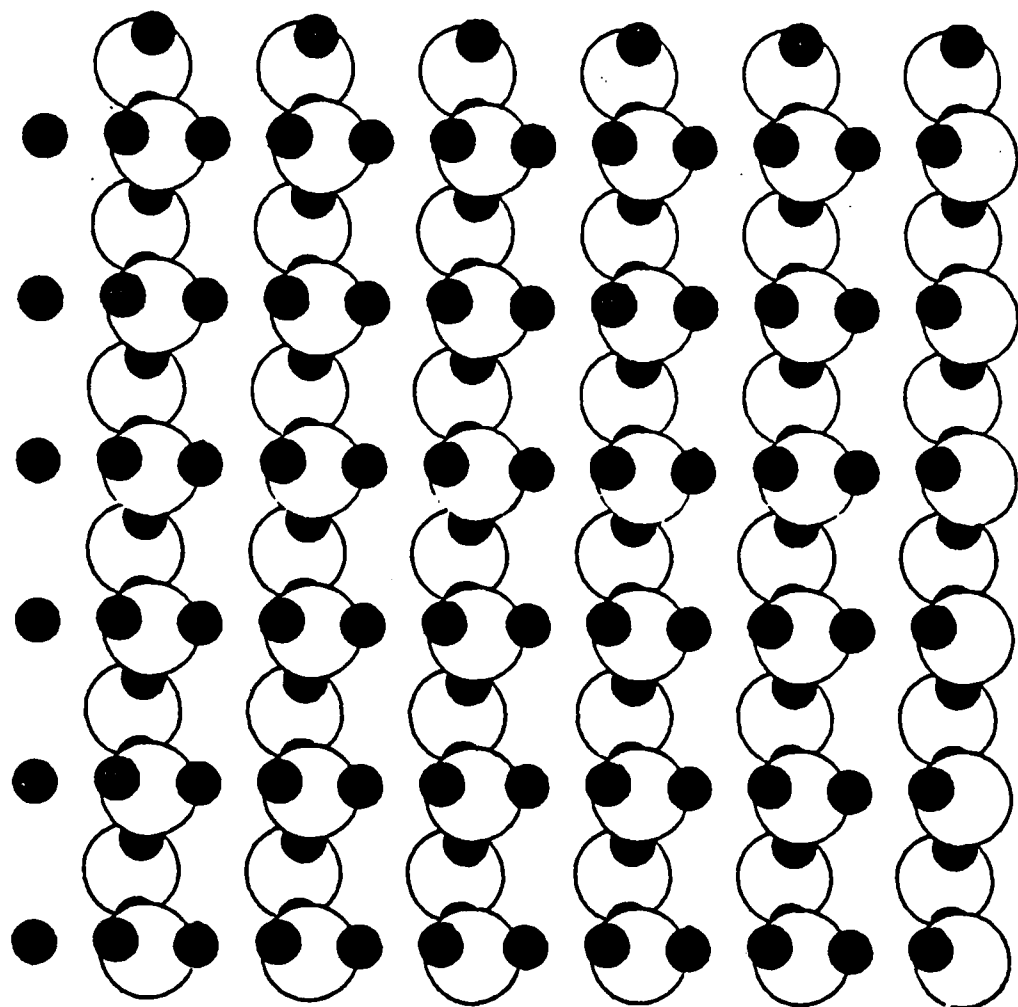


FIGURE 14a

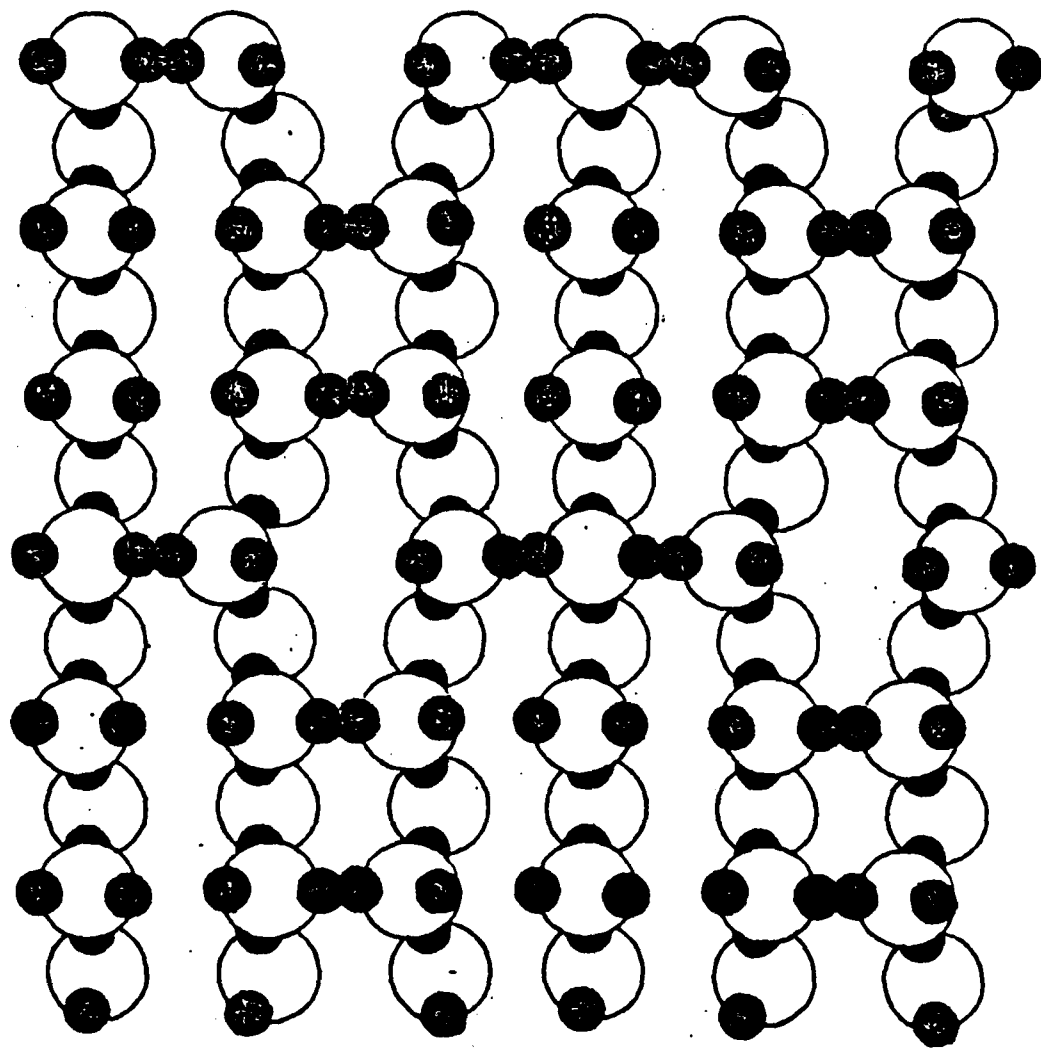


FIGURE 14b